

RESEARCH ARTICLE SUMMARY

CELL BIOLOGY

BAK/BAX macropores facilitate mitochondrial herniation and mtDNA efflux during apoptosis

Kate McArthur,* Lachlan W. Whitehead, John M. Heddleston, Lucy Li, Benjamin S. Padman, Viola Oorschot, Niall D. Geoghegan, Stephane Chappaz, Sophia Davidson, Hui San Chin, Rachael M. Lane, Marija Dramicanin, Tahnee L. Saunders, Canny Sugiana, Romina Lessene, Laura D. Osellame, Teng-Leong Chew, Grant Dewson, Michael Lazarou, Georg Ramm, Guillaume Lessene, Michael T. Ryan, Kelly L. Rogers, Mark F. van Delft, Benjamin T. Kile*

INTRODUCTION: There has been an explosion of interest in the role of cell death pathways and damage-associated molecular pattern (DAMP) signaling in shaping inflammatory and immune responses. Mitochondria are central to the intrinsic apoptosis pathway, the classical form of programmed cell death. Several mitochondrial constituents have been implicated as DAMPs, including mitochondrial DNA (mtDNA). Recent work has shown that activation of intrinsic BAK and BAX-mediated apoptosis results in mtDNA-dependent triggering of the innate immune cGAS/STING pathway, resulting in type I interferon production by dying cells. The apoptotic caspase cascade normally functions to suppress this mtDNA-induced cGAS/STING signaling, rendering apoptosis “immunologically silent.”

RATIONALE: It is thought that during apoptosis, mtDNA is released into the cytoplasm. In addition to apoptosis, loss of mtDNA from the matrix has been associated with conditions including HIV and dengue infection, calcium overload, irradiation, or inflammatory diseases such as systemic lupus erythematosus or rheumatoid arthritis. However, mtDNA escape from the mitochondria has not been documented in real time.

RESULTS: Using a combination of live-cell lattice light-sheet microscopy, 3D structured illumination microscopy, correlative light electron microscopy, and electron cryotomography, we found that after BAK/BAX activation and cytochrome c loss, the mitochondrial net-

work broke down and large BAK/BAX pores appeared in the outer membrane. These BAK/BAX macropores allowed the inner membrane an outlet through which it herniated, carrying with it mitochondrial matrix components, including the mitochondrial genome. A subset of the herniated inner membranes lost their integrity, allowing mtDNA to be exposed to the cytoplasm.

CONCLUSION: An extensive literature suggests that mtDNA is found outside the mitochondria—and, indeed, outside the cell—in a wide range of circumstances. Our study provides a mechanistic description of its release from the mitochondria. mtDNA release from mitochondria during apoptosis occurs irrespective of caspase activity, but in normal cells, caspases attenuate the subsequent cGAS/STING-mediated

interferon response by driving rapid cellular collapse and clearance. Mitochondrial herniation might represent a general mechanism of mtDNA escape.

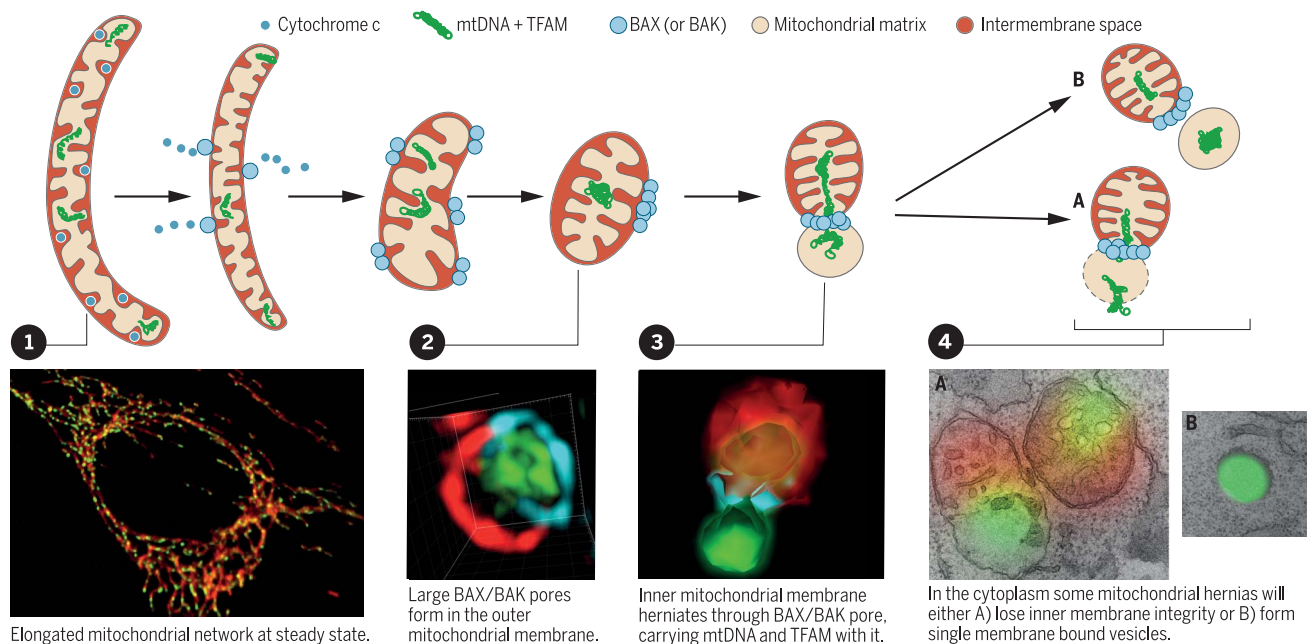
In addition to BAK and BAX oligomerization, there may be alternative triggers—for example, other pore-forming proteins (host- or pathogen-derived) or mitochondrial stresses—that lead to the occurrence of this phenomenon. ■

ON OUR WEBSITE

Read the full article at <http://dx.doi.org/10.1126/science.aao6047>

The list of author affiliations is available in the full article online.
*Corresponding author. Email: kate.mcarthur@monash.edu (K.M.); benjamin.kile@monash.edu (B.T.K.)
Cite this article as K. McArthur et al., *Science* 359, eaao6047 (2018). DOI: 10.1126/science.aao6047

Schematic of apoptotic mitochondrial herniation. Inset images show the key stages as captured by lattice light-sheet microscopy, structured illumination microscopy, and correlative light and electron microscopy.



RESEARCH ARTICLE

CELL BIOLOGY

BAK/BAX macropores facilitate mitochondrial herniation and mtDNA efflux during apoptosis

Kate McArthur,^{1,2,3*} Lachlan W. Whitehead,^{1,2} John M. Heddleston,⁴ Lucy Li,¹ Benjamin S. Padman,⁵ Viola Oorschot,⁶ Niall D. Geoghegan,^{1,2} Stephane Chappaz,^{1,2,3} Sophia Davidson,¹ Hui San Chin,¹ Rachael M. Lane,³ Marija Dramicanin,^{1,2} Tahnee L. Saunders,³ Canny Sugiana,³ Romina Lessene,^{1,2} Laura D. Osellame,⁵ Teng-Leong Chew,⁴ Grant Dewson,^{1,2} Michael Lazarou,⁵ Georg Ramm,^{5,6} Guillaume Lessene,^{1,2,7} Michael T. Ryan,⁵ Kelly L. Rogers,^{1,2} Mark F. van Delft,^{1,2} Benjamin T. Kile^{1,2,3*}

Mitochondrial apoptosis is mediated by BAK and BAX, two proteins that induce mitochondrial outer membrane permeabilization, leading to cytochrome c release and activation of apoptotic caspases. In the absence of active caspases, mitochondrial DNA (mtDNA) triggers the innate immune cGAS/STING pathway, causing dying cells to secrete type I interferon. How cGAS gains access to mtDNA remains unclear. We used live-cell lattice light-sheet microscopy to examine the mitochondrial network in mouse embryonic fibroblasts. We found that after BAK/BAX activation and cytochrome c loss, the mitochondrial network broke down and large BAK/BAX pores appeared in the outer membrane. These BAK/BAX macropores allowed the inner mitochondrial membrane to herniate into the cytosol, carrying with it mitochondrial matrix components, including the mitochondrial genome. Apoptotic caspases did not prevent herniation but dismantled the dying cell to suppress mtDNA-induced innate immune signaling.

The mitochondrial, or intrinsic, apoptosis pathway is governed by the interplay among members of the BCL-2 family of proteins, which mediate mitochondrial integrity (1, 2). At steady state, pro-survival BCL-2 members (e.g., MCL-1 and BCL-X_L) restrain the activity of pro-death BAK and BAX. In response to developmental cues and stress signals, pro-survival activity is overwhelmed, permitting BAK and BAX activation. BAK and BAX oligomerize in the mitochondrial outer membrane, causing its permeabilization and the release of apoptogenic factors, of which the best characterized is cytochrome c (3, 4). Cytoplasmic cytochrome c forms part of the apoptosome complex, which successively activates caspase-9 and the apoptotic effector caspases, caspase-3 and caspase-7. Together, these proteases efficiently cleave a multitude of

substrates within the cell to accelerate its demise (5).

Apoptosis, unlike other forms of cell death such as necroptosis or pyroptosis, is generally thought to be an immunologically silent process, thereby providing a mechanism for cell clearance and tissue homeostasis that does not provoke a potentially damaging inflammatory or immune response. Immunological silence requires a functional apoptotic caspase cascade (6, 7). Genetic ablation or pharmacological inhibition of the caspase cascade during BAK/BAX-mediated apoptosis results in the production of the potent antiviral cytokine interferon- β (IFN- β). This is the result of mitochondrial DNA (mtDNA) triggering the activation of the cGAS/STING (cyclic guanosine monophosphate/adenosine monophosphate synthase/stimulator of interferon genes) signaling pathway, a cytosolic component of the cell's innate immune system designed to detect pathogen-derived DNA. In the absence of active caspases, mtDNA is recognized as a damage-associated molecular pattern (DAMP), and the dying cell behaves as if it were virally infected.

How cGAS gains access to the mitochondrial genome during apoptosis remains unknown, but the fact that mtDNA is enriched in cGAS immunoprecipitates from cells undergoing caspase-inhibited apoptosis suggests that the two do interact (6). The simplest explanation is that mtDNA is released into the cytoplasm. Multiple

studies have found evidence of mtDNA release from damaged mitochondria. mtDNA fragments are seen in the cytoplasmic fractions of cells induced to undergo death by calcium overload or irradiation, which has been ascribed to opening of the so-called mitochondrial permeability transition pore (MPTP) (8, 9). Cytosolic mtDNA fragments are also found in cells experiencing mitochondrial stress (10) or inflammasome activation (11); however, the mechanism of mtDNA release in these settings is not clear. It has been postulated that apoptosis is a key upstream requirement, because overexpression of BCL-2 attenuated downstream mtDNA-induced NLRP3 activation (11). Despite this finding and those in the earlier reports (6, 7), the notion that BAK and BAX might directly mediate mtDNA efflux remains controversial (12). Furthermore, although it is generally accepted that mtDNA would activate DNA sensors upon its release into the cytoplasm, mtDNA release itself has not been demonstrated in real time (13).

mtDNA is released from apoptotic mitochondria

To establish whether mtDNA is released into the cytosol during intrinsic apoptosis, we imaged immortalized mouse embryonic fibroblasts (MEFs) with live-cell lattice light-sheet microscopy (LLSM) (14). Wild-type MEFs are dependent on the pro-survival proteins MCL-1 and BCL-X_L for survival. MEFs lacking MCL-1 undergo BAK/BAX-dependent apoptosis in response to the BH3 mimetic drug ABT-737, a potent inhibitor of BCL-X_L and BCL-2 (15, 16) (Fig. 1A). To visualize mitochondria, we stably transduced *Mcl1*^{-/-} MEFs with a vector encoding the mitochondrial outer-membrane protein TOMM20 bearing a HaloTag (TOMM20-Halo), which fluoresces upon addition of the cell-permeant HaloTag-specific dye JaneliaFluor-646 (17). mtDNA was detected by coexpression of the mtDNA-binding protein TFAM (transcription factor A, mitochondrial), which was tagged with the green fluorescent protein (GFP) variant mNeonGreen (18) (Fig. 1B). At steady state, mitochondria formed an elaborate network, throughout which individual mtDNA nucleoids were evenly distributed (Fig. 1C). Upon addition of ABT-737, this network underwent an almost immediate dissolution, breaking down within several minutes of the onset of apoptosis (Fig. 1D). Coincident with this process, TFAM-positive nucleoids coalesced within mitochondria. As mitochondria condensed into discrete globular structures, we observed nucleoids being released into the cytoplasm (Movie 1). This phenomenon was remarkably consistent in its form and kinetics. Moreover, it occurred in both the presence and absence of the pan-caspase inhibitor QVD-OPH (19). When apoptotic cells were co-incubated with QVD-OPH, they remained attached to the coverslip, allowing continuous imaging for up to 1 hour. In contrast, without caspase inhibition, cells rapidly contracted and detached from the coverslip immediately after nucleoid release (Fig. 1E and Movie 2).

¹Walter and Eliza Hall Institute of Medical Research, Parkville, Victoria, Australia. ²Department of Medical Biology, University of Melbourne, Parkville, Victoria, Australia. ³Anatomy and Developmental Biology, Monash Biomedicine Discovery Institute, Monash University, Melbourne, Victoria, Australia. ⁴Advanced Imaging Center, Howard Hughes Medical Institute, Janelia Research Campus, Ashburn, VA, USA. ⁵Biochemistry and Molecular Biology, Monash Biomedicine Discovery Institute, Monash University, Melbourne, Victoria, Australia. ⁶Monash Ramaciotti Centre for Cryo Electron Microscopy, Monash University, Melbourne, Victoria, Australia. ⁷Department of Pharmacology and Therapeutics, University of Melbourne, Parkville, Victoria, Australia.

*Corresponding author. Email: kate.mcarthur@monash.edu (K.M.); benjamin.kile@monash.edu (B.T.K.)

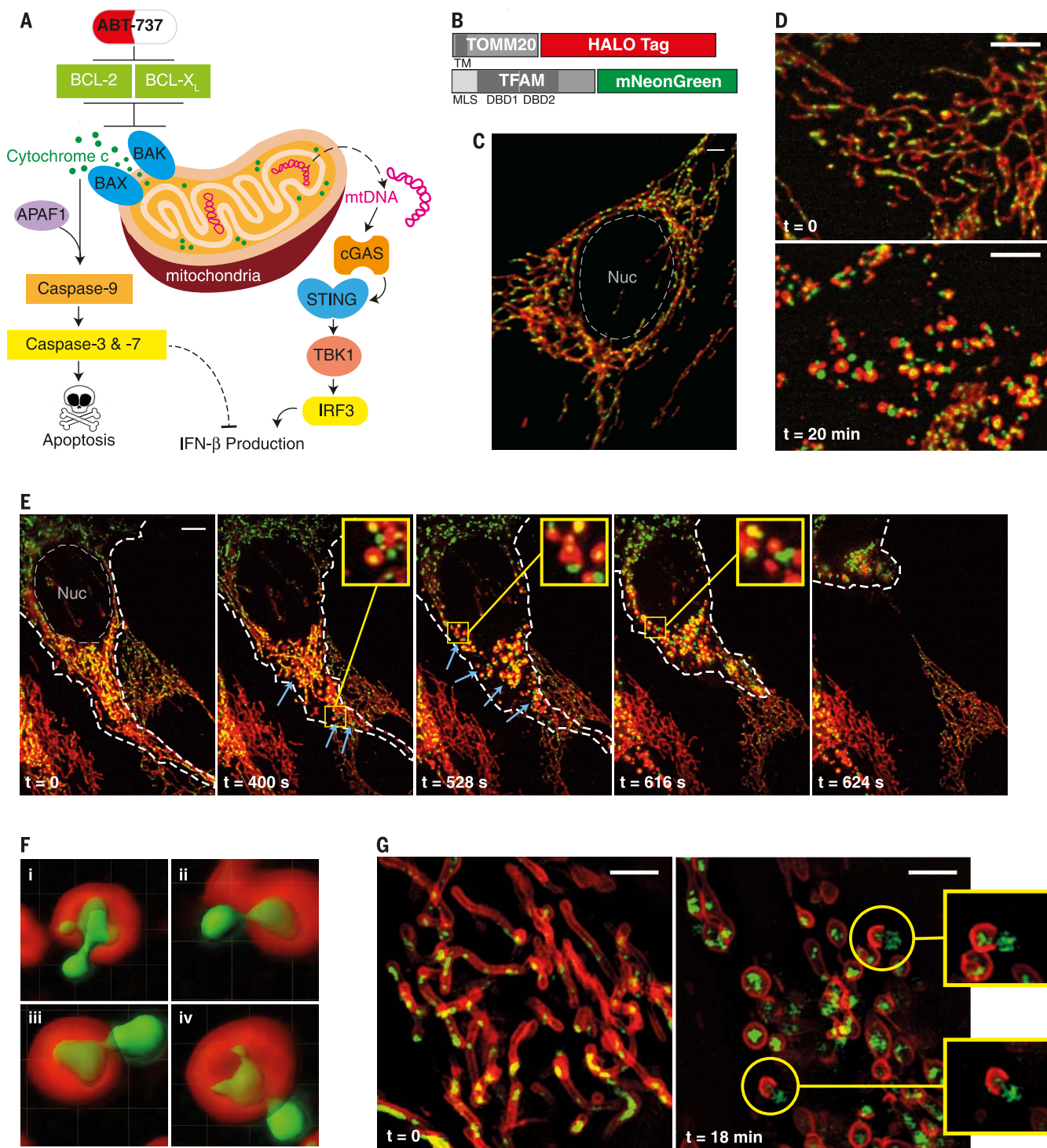


Fig. 1. mtDNA is released from apoptotic mitochondria. (A) Apoptotic interferon production pathway. APAF1, apoptotic protease activating factor 1; TBK1, TANK binding kinase 1; IRF3, interferon regulatory factor 3.

(B) Fluorescent fusion proteins used to visualize mitochondria (TOMM20-Halo) and mtDNA (TFAM-mNeonGreen). TM, transmembrane domain; MLS, mitochondrial localization sequence; DBD1 and DBD2, DNA binding domain-1 and -2. (C) Typical staining of mitochondrial network in *Mcl1*^{-/-} MEFs at steady state, as imaged by LLSM, showing mitochondria (red, TOMM20-Halo) and mtDNA (green, TFAM-mNeonGreen). (D) Still snapshots of nucleoid efflux before and 20 min after ABT-737 (500 nM) + QVD-OPh (20 μ M) treatment, as imaged by LLSM (see Movie 1). (E) Snapshots from LLSM of

Mcl1^{-/-} MEFs undergoing apoptosis with active caspase cascades; elapsed time after ABT-737 (500 nM) treatment is indicated (see Movie 2). The cell is outlined by a dashed white line. Blue arrows highlight nucleoid externalization events. (F) Multiple examples [(i) to (iv)] of single mitochondria undergoing nucleoid efflux from LLSM movies in (D), displayed using 3D surface reconstructions overlaid upon original data with Imaris software. (For 3D surface reconstructions of the full time lapse, see Movie 3.) (G) 3D-SIM imaging of nucleoid externalization under the same conditions as (D) (see Movie 4). Insets show mitochondria during nucleoid efflux. Scale bars, 5 μ m [(C) to (E)], 2 μ m (G). Data in (D), (E), and (G) are representative of at least three independent experiments.

Three-dimensional (3D) surface reconstruction revealed that nucleoid release occurred from a single site on mitochondrial fragments. TFAM-positive nucleoids formed barbell-shaped structures during the release process, suggesting physical constriction at the mitochondrial surface (Fig. 1F and Movie 3). Intriguingly, nucleoids remained in close proximity to the mitochondria from which they had exited. These patterns of constriction through single exit points were confirmed in more detail by live 3D structured illumination microscopy (3D-SIM), which clearly demonstrated nucleoid release from mitochondria

with a “cup-like” appearance (Fig. 1G and Movie 4). Similar results were obtained in human HeLa cells incubated with a combination of ABT-737 and the MCL-1 inhibitor S63845 (20) (fig. S1A), or in MEFs when mtDNA was visualized with the DNA dye PicoGreen (21) (fig. S1B). Given the propensity of the latter to photobleach, we focused on the TFAM mtDNA reporter system for further investigation.

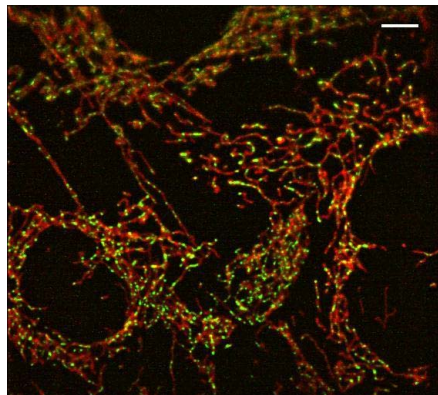
Cytochrome c loss precedes mtDNA efflux

To understand the temporal relationship between mtDNA release and other events during mitochondrial apoptosis, we used LLSM to image MEFs coexpressing TOMM20-Halo, TFAM-Tomato, and cytochrome c-GFP (Fig. 2A and Movie 5). Upon treatment with ABT-737 and QVD-OPh, cytochrome c loss from mitochondria was clearly evident. Consistent with previous reports (22–26), it occurred rapidly in a wave-like fashion across the mitochondrial network, over a period of 30 to 90 s. Cytochrome c efflux preceded mitochondrial network dissolution and subsequent mtDNA release, the kinetics of which were quantified using custom automated FLJI

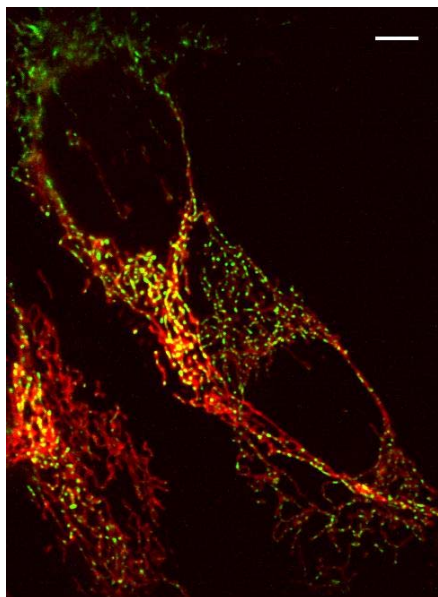
(27) scripts (Fig. 2, B to D, and fig. S2, A and B). This combination of visual and quantitative analysis clearly identified BAK/BAX-mediated cytochrome c release as the first event, with mitochondrial morphological rearrangement and mtDNA efflux occurring consecutively thereafter. The relative timing of each event was remarkably consistent between individual cells and across independent experiments (Fig. 2E). To further confirm that loss of cytochrome c precedes nucleoid release, we conducted a kinetic analysis in which cells were treated, fractionated, and immunoblotted to observe the timing of cytochrome c and TFAM appearance in the cytosol of apoptotic cells. Full release of cytochrome c was observed as early as 0.5 to 1 hour (Fig. 2F). TFAM was detected in the cytosol after 4 and 6 hours [as was another matrix component, dihydrolipoamide dehydrogenase (DLD)]—time points at which IFN- β was present in supernatants (Fig. 2G).

Mitochondrial dynamics and mtDNA release

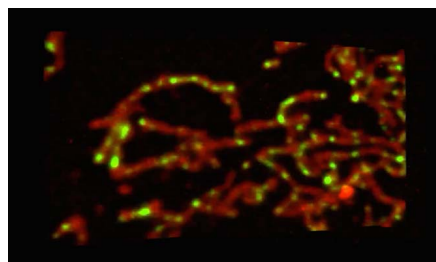
To maintain a healthy network, mitochondria continuously undergo fission and fusion (28–31).



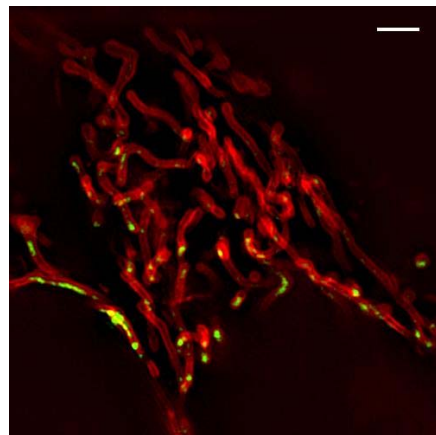
Movie 1. Lattice light-sheet imaging of mitochondria (red, TOMM20-Halo) and mtDNA (green, TFAM-mNeonGreen) from *Mcl1*^{-/-} MEFs undergoing apoptosis induced by ABT-737 and QVD-OPh. Images were captured at a rate of one 3D volume every 8 s.



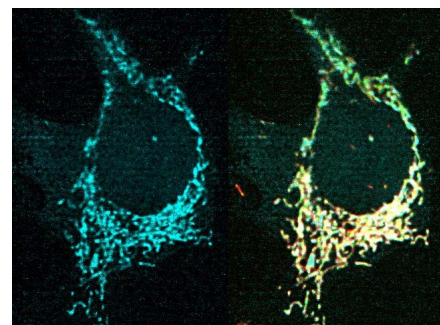
Movie 2. Lattice light-sheet imaging of mitochondria (red, TOMM20-Halo) and mtDNA (green, TFAM-mNeonGreen) from *Mcl1*^{-/-} MEFs undergoing apoptosis with active caspases induced by ABT-737 treatment alone. Images were captured at a rate of one 3D volume every 8 s.



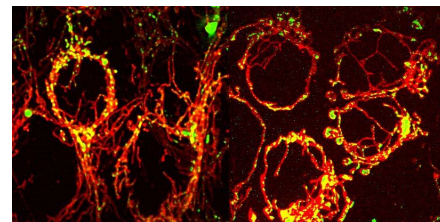
Movie 3. 3D surface reconstruction generation (red, mitochondria; green, mtDNA nucleoids) using Imaris software, which highlights mtDNA release events in Movie 1.



Movie 4. 3D SIM imaging of mitochondria (red, TOMM20-Halo) and mtDNA (green, TFAM-mNeonGreen) from *Mcl1*^{-/-} MEFs undergoing apoptosis induced by ABT-737 and QVD-OPh. Images were captured at a rate of one 3D volume every 60 s.



Movie 5. Lattice light-sheet imaging of mitochondria (red, TOMM20-Halo), mtDNA (green, TFAM-mNeonGreen), and cytochrome c (blue) from *Mcl1*^{-/-} MEFs undergoing apoptosis induced by ABT-737 and QVD-OPh. Images were captured at a rate of one 3D volume every 13 s.



Movie 6. Lattice light-sheet imaging of mitochondria (red, TOMM20-Halo) and mtDNA (green, TFAM-mNeonGreen) from DRP1-deficient MEFs undergoing apoptosis induced by ABT-737 and QVD-OPh. Left: *Mcl1*^{CRISPR/-/-}*Drp1*^{-/-} MEFs derived from *Drp1* knockout mice. Right: *Mcl1*^{-/-}*Drp1*^{CRISPR/-/-} MEFs generated by CRISPR/Cas9 targeting of *Drp1*. Images were captured at a rate of one 3D volume every 13 s.

In mammals, the former is mediated by dynamin-related protein-1 (DRP1) (32, 33), the latter by optic atrophy protein-1 (OPA1) and mitofusin-1 and -2 (MFN1 and MFN2) (34, 35). Mitochondrial fragmentation during apoptosis has been widely documented (36–39), and a large body of evidence suggests that the response to various apoptotic stimuli is altered when fission or fusion are inhibited (40–43) [reviewed in (44)]. However, the precise requirement for fission (in particular) in mitochondrial apoptosis and its temporal relationship to cytochrome c release remains controversial (45–47).

To establish whether fission and/or fusion facilitate apoptotic mtDNA release, we generated *Drp1*^{−/−} *Mcl1*^{−/−}, *Opal*^{−/−} *Mcl1*^{−/−}, and *Mfn1*^{−/−} *Mcl1*^{−/−} MEFs and imaged these cells by LLSM. Consistent with their established role in fusion (48–50), loss of either OPA1 or MFN1/

MFN2 resulted in hyperfragmented mitochondria at steady state (fig. S3A). *Opal*^{−/−} *Mcl1*^{−/−} and *Mfn1*^{−/−} *Mfn2*^{−/−} *Mcl1*^{−/−} cells exhibited a modest increase in sensitivity to ABT-737, readily undergoing cytochrome c release and nucleoid efflux in response to ABT-737 (Fig. 3, A to D, and fig. S3, B to D). In contrast, and as previously reported (51, 52), fission-deficient *Drp1*^{−/−} cells at steady state exhibited a hyperfused mitochondrial network (fig. S3A). The behavior of this network, upon induction of BAK/BAX-mediated apoptosis, was cell line-dependent. In MEFs derived from knockout mice, marked mitochondrial rearrangement was observed, but it was incomplete, with mitochondria exhibiting a “beads-on-a-string” appearance and only a limited number releasing mtDNA (Fig. 3, E and F, fig. S3F, and Movie 6). Strikingly, mtDNA release was observed only from discrete globular mitochondria,

of which there were fewer in the absence of DRP1. In contrast, when we induced apoptosis in independently derived CRISPR/Cas9 *Drp1*-targeted MEF subclones (deletion confirmed by imaging and immunoblot; fig. S3H), mitochondrial network breakdown was equivalent to that seen in wild-type counterparts (Fig. 3E and Movie 6). However, regardless of the disparities in mitochondrial dynamics, in all DRP1-deficient lines tested, we observed robust cGAS-dependent IFN-β secretion during caspase-inhibited apoptosis (fig. S3, E and G). Thus, loss of DRP1 does not prevent mtDNA-induced DAMP signaling.

mtDNA is released through BAK/BAX foci

We thus revisited the proposed involvement of the MPTP in facilitating this process (8). The exact nature and composition of the MPTP remains controversial; currently, it is defined by the

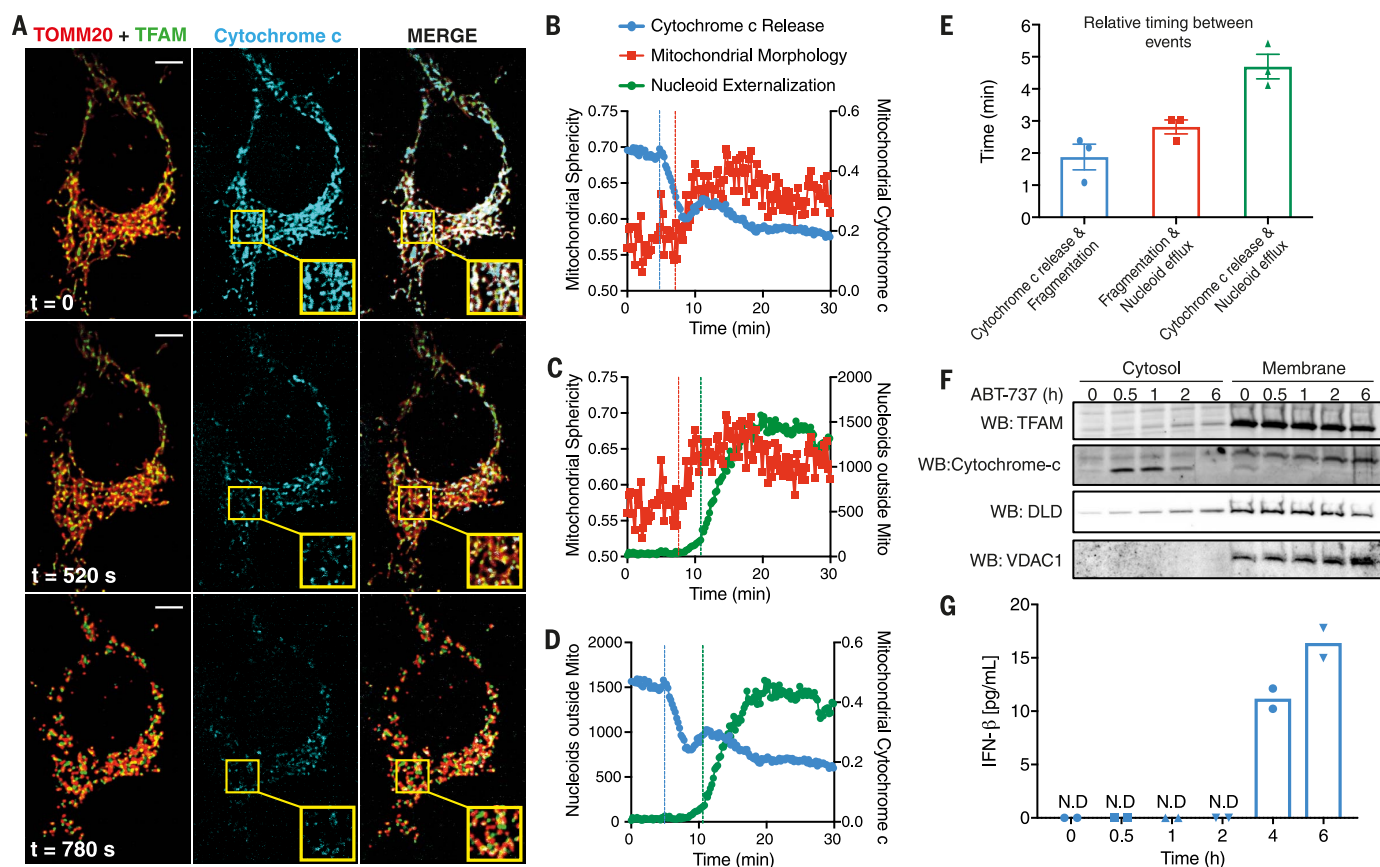


Fig. 2. Cytochrome c loss precedes mtDNA efflux. (A) Snapshots from LLSM imaging of *Mcl1*^{−/−} MEFs expressing TOMM20-Halo (stained with JF-646) (red), TFAM-tdTomato (green), and cytochrome c-GFP (blue), with cytochrome c loss and externalized nucleoids apparent 520 s and 780 s, respectively, after ABT-737 (500 nM) + QVD-Oph (20 μM) treatment (see Movie 5). Scale bars, 5 μm. (B to D) Kinetic quantitation of LLSM imaging in (A), representative of three independent experiments, depicting the relative timing between mitochondrial fragmentation and cytochrome c loss (B), mitochondrial fragmentation and nucleoid externalization (C), and cytochrome c loss and nucleoid externalization (D). Dashed vertical lines indicate the time at which each event begins, as determined visually from time-lapse movies. Parameters used to quantitate events are mitochondrial sphericity (reflective of morphology changes; values range between 0 = linear

and 1 = sphere), area of cytochrome c signal inside mitochondria (pixels) relative to mitochondrial area (pixels) (reflective of cytochrome c loss to the cytoplasm), and number of mtDNA nucleoids outside mitochondria. (E) Graphical representation of relative timing between the initiation of each event (cytochrome c loss, mitochondrial fragmentation, and externalized nucleoids) across three separate imaging experiments. Data are means ± SEM. (F) Western blots of cytosolic (left) and membrane (right) fractions of *Mcl1*^{−/−} MEFs pretreated with QVD-Oph (50 μM) followed by ABT-737 (1 μM) at the indicated times. DLD, dihydrolipoamide dehydrogenase (matrix protein); VDACL1, voltage-dependent anion-selective channel 1 (OMM protein). (G) IFN-β in culture supernatants from *Mcl1*^{−/−} MEFs in (F) collected immediately before fractionation. Blots and data in (F) and (G) are representative of two or three independent experiments. N.D., not detected.

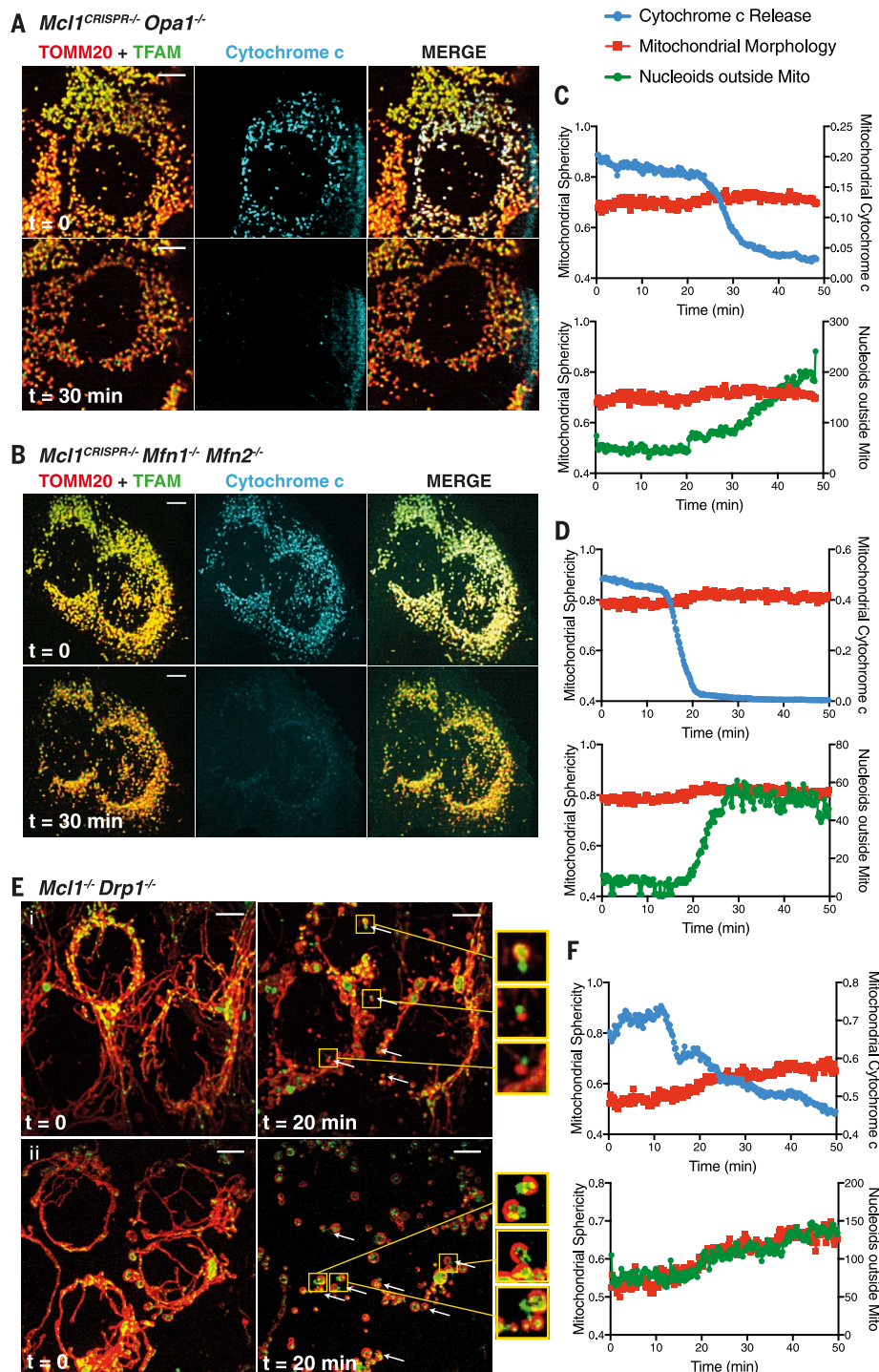
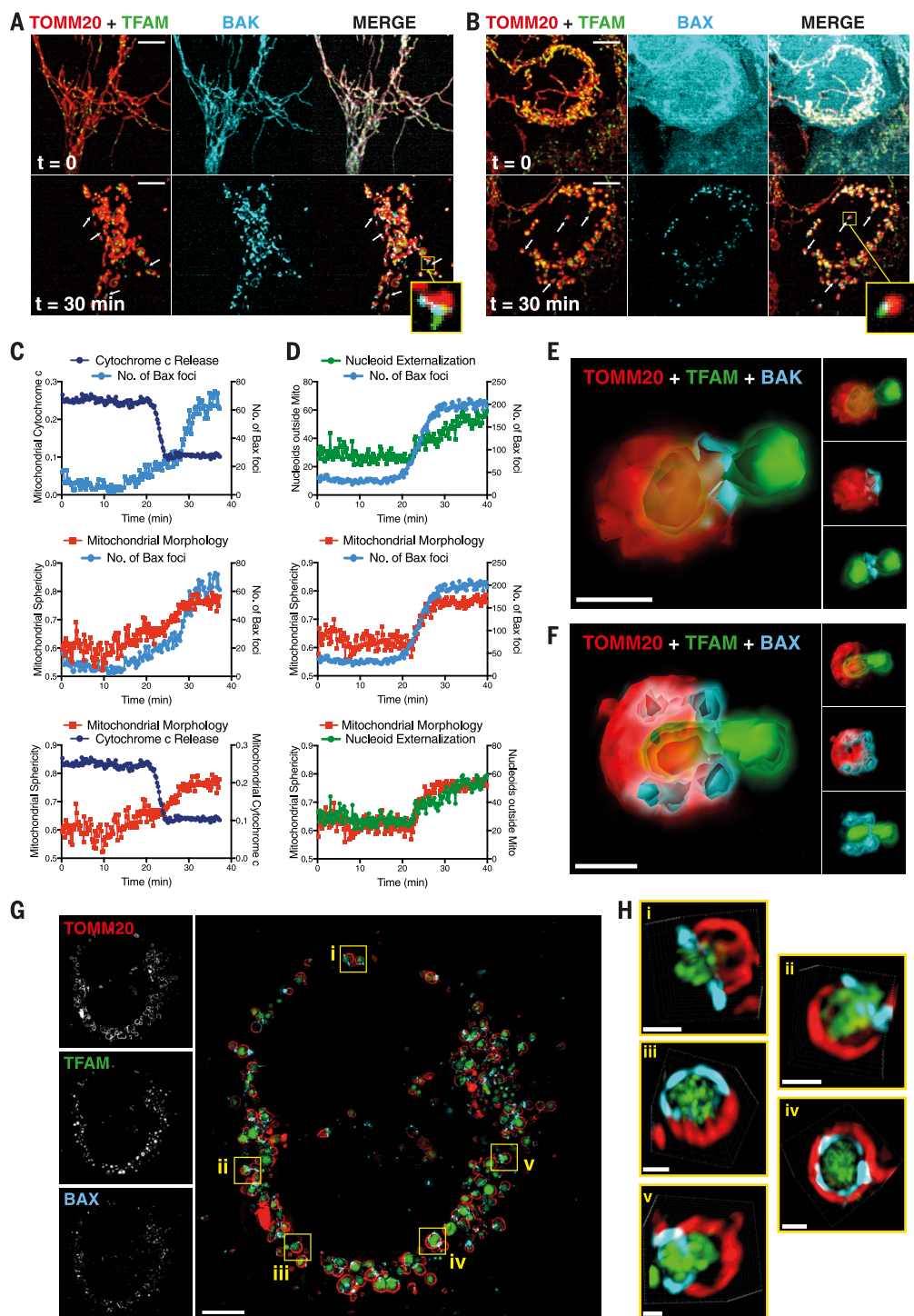


Fig. 3. Breakdown of mitochondrial network and mtDNA release during apoptosis does not require DRP1 or the mitochondrial fusion machinery. (A and B) Apoptotic mtDNA release from fusion-deficient *Mcl1^{CRISPR-/-} Opa1^{-/-}* MEFs (A) and *Mcl1^{CRISPR-/-} Mfn1^{-/-} Mfn2^{-/-}* MEFs (B) 30 min after ABT-737 (500 nM) + QVD-OPh (20 μ M) treatment, as imaged by LLSM. (C and D) Kinetic quantitation of (A) and (B), respectively. (E) Two examples of mitochondrial fragmentation during apoptosis in *MCL1/DRP1*-deficient MEFs 20 min after ABT-737 (1 μ M) + QVD-OPh (20 μ M) treatment, as imaged by LLSM. Top: *Mcl1^{CRISPR-/-} Drp1^{-/-}* MEFs derived from *Drp1* knockout mice. Bottom: *Mcl1^{CRISPR-/-} DRP1^{-/-}* MEFs generated by CRISPR/Cas9 targeting of *Drp1*. mtDNA release events are highlighted by white arrows (see Movie 6). Scale bars in (A), (B), and (E), 5 μ m. (F) Kinetic quantitation of apoptotic mtDNA release from fission-deficient *Mcl1^{-/-} DRP1^{-/-}* MEFs, showing the relative timing of mitochondrial fragmentation, cytochrome c loss, and nucleoid externalization. All images and graphs are representative of three independent experiments.

ability of the drug cyclosporin A (CsA) to block its opening (53, 54). When we pretreated MEFs with CsA and then induced apoptosis, we saw identical patterns and amounts of nucleoid efflux (fig. S4, A and B). This indicated that apoptotic mtDNA efflux does not require MPTP opening. To assess mitochondrial membrane potential during herniation, we stained cells with the membrane potential dye TMRM and imaged them via LLSM. When treated with ABT-737 and QVD-OPh, all mitochondria rapidly lost TMRM staining (fig. S2, C and D). This occurred before mitochondrial morphology rearrangement and mtDNA release. In contrast, treatment of cells with the uncoupling agents actinomycin A and oligomycin A (A/O) triggered a drastic loss of TMRM staining but did not lead to mitochondrial morphology changes or mtDNA release (fig. S2, C and D). Accordingly, A/O treatment did not induce IFN- β production from MEFs (fig. S2E). Thus, although mitochondria lose membrane potential during caspase-inhibited apoptosis, loss of potential in itself does not trigger mtDNA release. We therefore considered the possibility that BAK and BAX directly facilitate this process.

It is well established that activation of BAK and BAX leads to their oligomerization in the outer mitochondrial membrane (OMM) and its subsequent permeabilization (40, 55–58). However, they are not thought to rupture the inner mitochondrial membrane (IMM) (59). We thus examined the localization of BAK and BAX during mtDNA release. LLSM imaging of *Bak^{-/-} Bax^{-/-} Mcl1^{-/-}* MEFs reconstituted with a tagged variant of BAK (BAK-mRuby2), in addition to TOMM20-Halo and TFAM-mNeonGreen, revealed uniform BAK staining across the mitochondria. Upon induction of apoptosis, BAK became concentrated in bright foci in the OMM (Fig. 4A). In cells reconstituted with a tagged variant of BAX (BAX-mRuby2), BAX staining was ubiquitous at steady state, consistent with its reported cytoplasmic location. In response to ABT-737, BAX was very clearly recruited to, and also formed bright foci in, fragmented mitochondria (Fig. 4B and Movie 7). In both cases, these large aggregates of BAK or BAX—which were similar in scale and topology to those previously described using stimulated emission depletion microscopy or single-molecule localization microscopy (60, 61)—appeared 4 to 8 min after cytochrome c loss (Fig. 4C, top), concurrent with mitochondrial morphology changes and nucleoid release (Fig. 4D, middle and bottom). Given that cytochrome c release precedes fragmentation and mtDNA efflux (Fig. 2), this suggests that cytochrome c must exit from BAK or BAX pores too small to be resolved by LLSM. This idea is consistent with a model (62) whereby only a small amount of BAX is required for mitochondrial outer membrane permeabilization (MOMP) and the majority is recruited after cytochrome c release has taken place. mtDNA release was observed only after large BAK/BAX foci had appeared, and these BAK/BAX foci were present at the same location from which mtDNA was released (Fig. 4, A and B, white arrows). 3D visualization clearly showed BAK and BAX encircling the point of

Fig. 4. mtDNA is released from BAK/ BAX foci. (A and B) Representative snapshots from LLSM imaging of *Mcl1*^{-/-} *Bak*^{-/-} *Bax*^{-/-} MEFs overexpressing TOMM20-Halo (red), TFAM-mNeonGreen (green), and reexpressing mRuby2-BAK (A) or mRuby2-BAX (B) (blue), before and after mtDNA release 30 min after ABT-737 (10 μ M) + QVD-OPh (20 μ M) treatment (see Movie 7). Scale bars, 5 μ m. (C) Kinetic quantitation of the appearance of BAX foci with respect to cytochrome c release and fragmentation of mitochondria events (mitochondrial sphericity measurement) from LLSM imaging of *Mcl1*^{-/-} *Bak*^{-/-} *Bax*^{-/-} MEFs expressing TOMM20-Halo, mRuby2-BAX, and cytochrome c-GFP. (D) Kinetic quantitation of the appearance of BAX foci with respect to nucleoid externalization and mitochondrial fragmentation events from LLSM imaging of *Mcl1*^{-/-} *Bak*^{-/-} *Bax*^{-/-} MEFs expressing TOMM20-Halo, mRuby2-BAX, and TFAM-mNeonGreen. Data in (C) and (D) are representative of three independent experiments. (E and F) Single mitochondria undergoing nucleoid externalization from LLSM movies, displayed using 3D surface reconstructions overlaid upon original data with Imaris software. Scale bars, 500 nm. (G) 3D-SIM imaging of *Mcl1*^{-/-} *Bak*^{-/-} *Bax*^{-/-} MEFs expressing TOMM20-Halo (stained with JF-646), mScarlet-BAX, and TFAM-mNeonGreen, 90 min after ABT-737 (10 μ M) + QVD-OPh (20 μ M) treatment. Overview image is a maximum projection of the SIM reconstruction, with selected examples where clear BAX rings were evident [boxed and labeled (i) to (v)]. Image is representative of 20 images taken over the course of three independent experiments. Scale bar, 4 μ m. (H) 3D snapshots of single mitochondria undergoing nucleoid externalization from the SIM image in (G). Scale bars, 500 nm.



mtDNA constriction and exit from fragmented mitochondria (Fig. 4, E and F, and fig. S4, C and D). This was confirmed at higher resolution by 3D-SIM (Fig. 4, G and H, and fig. S4E).

mtDNA release is the result of IMM herniation

mtDNA nucleoids are located in the matrix of the mitochondria, insulated from the cytosol by two membranes, the inner and outer. Thus, our data raised the question of how mtDNA

might make its way from the matrix to the cytoplasm via an OMM pore. To address this, we examined the behavior of a fluorophore targeted to the space within the mitochondrial matrix (MMX-Tomato) expressed in *Mcl1*^{-/-} MEFs (fig. S5A). Upon treatment with ABT-737, MMX-Tomato exited the mitochondria in a manner similar to that of mtDNA: It was constricted during its release from a single discrete point, after which it remained in close proximity to the mitochondria, rather than dispersing throughout

the cytoplasm as we had anticipated (fig. S5B). This suggested the presence of an additional barrier restricting its egress to the cytoplasm. The obvious candidate for this was the IMM. We thus fluorescently labeled the IMM protein Distal Module Assembly Component-1 (63) (DMAC1-Tomato) and followed its localization during mtDNA release. LLSM imaging revealed that the majority of IMM remained localized with the OMM signal after mtDNA release (i.e., remained inside fragmented mitochondria) (fig. S5C).

Given that the resolution of LLSM is diffraction-limited (14), we again used higher-resolution live 3D-SIM and imaged cells expressing DMAC1-Tomato and TOMM20-Halo [stained with JF-546 (17)] to visualize both mitochondrial membranes. These studies revealed ultrathin DMAC1-containing “blisters” encapsulating mtDNA external to the OMM (Fig. 5, A and B). This suggested that the IMM herniates through macropores formed by BAK and BAX. To examine this in more detail, we conducted immunogold transmission electron microscopy (TEM) and electron cryotomography (ECT) studies of ABT-737-treated *Mcl1*^{-/-} MEFs. For TEM, mtDNA was visualized by the expression of GFP-tagged TFAM and immunogold la-

beling via an antibody to GFP. The TEM images revealed multiple instances where the OMM had peeled away from the IMM (Fig. 5C, ii), and others where the OMM clearly terminated while the IMM continued, ballooning out and encapsulating the mtDNA-TFAM signal (Fig. 5C, iii and iv). ECT confirmed the mitochondrial herniation event (Fig. 5, D and E). The advantages of ECT are enhanced resolution, elimination of any potential for sectioning artifacts, and 3D visualization (Movie 8). Thus, these data indicate that as a consequence of BAK/BAX OMM permeabilization, mitochondria fragment and larger BAK/BAX foci assemble. The formation of these BAK/BAX macropores elicits IMM herniation.

Immunoprecipitation of cGAS from apoptotic cells enriches for mtDNA (6). In considering the mechanism by which this interaction occurs, we wondered whether cGAS might localize to herniated mitochondria, potentially translocating across the IMM. To establish whether cGAS localizes to mitochondrial hernias, we initially conducted LLSM studies of *Mcl1*^{-/-} *cGAS*^{CRISPR/-} MEFs reconstituted with cGAS-GFP. At steady state, cGAS staining was diffuse throughout the cytoplasm. We added ABT-737 and imaged for 1 hour. Mitochondrial network breakdown and herniation occurred, but no change in cGAS localization was observed. To establish whether cGAS might localize to hernias at later time

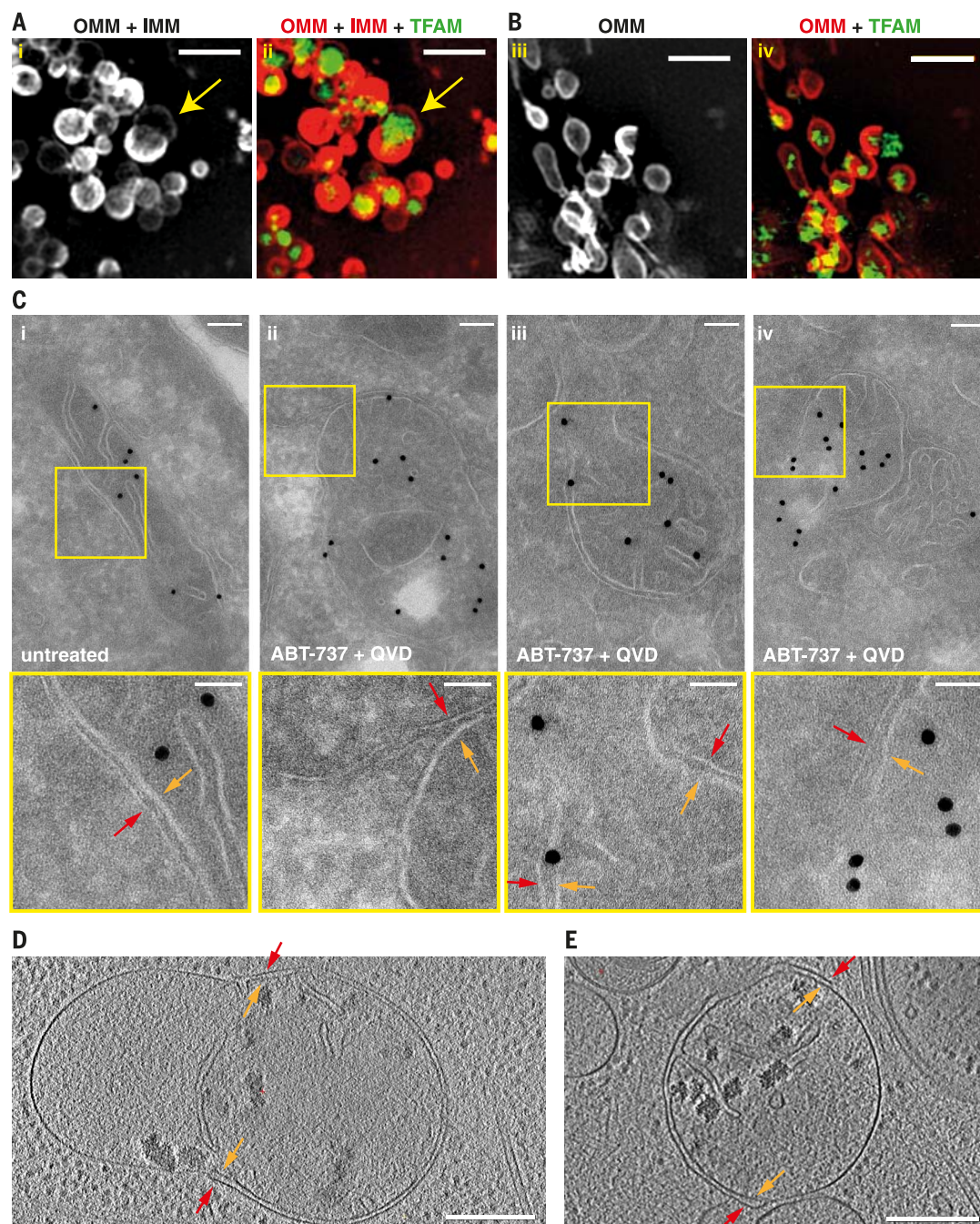


Fig. 5. mtDNA release occurs via inner mitochondrial membrane herniation. (A and B) 3D-SIM imaging of *Mcl1*^{-/-} MEFs expressing TOMM20-Halo (stained with JF-546) and TFAM-mNeonGreen, with additional DMAC1-Tomato [(i) and (ii)], representative of three independent experiments. For ease of comparison, 3D-SIM images from Fig. 1G (where only the OMM and mtDNA were stained) are included in (B). Joint IMM and OMM staining [(i), or red in (ii)] shows thin membrane (yellow arrows) encapsulating mtDNA [TFAM, green, (ii)] that is not present when OMM is stained alone [compare with (iii) and (iv)]. Scale bars, 2 μ m. (C) Electron microscopy imaging of untreated (i) or apoptotic mitochondria [(ii), (iii), and (iv)] immunogold-labeled for anti-GFP-TFAM to visualize location of mtDNA (black spots). Insets are annotated with arrows to mark areas where IMM (orange) and OMM (red) are clearly shown together [(i), untreated], peeling away from one another (ii), or during herniation where OMM clearly stops [(iii) and (iv)]. Scale bars, 100 nm (main images), 50 nm (insets). (D and E) ECT images of apoptotic mitochondria 90 min after ABT-737 (1 μ M) + QVD-OPh (20 μ M) treatment. Tomographic 10-nm slices are shown; arrows mark areas where OMM (red) clearly stops while IMM (orange) continues. Scale bars, 250 nm. See also Movie 8.

points, we conducted a 6-hour time course and imaged cells by confocal microscopy. At 4 and 6 hours after the induction of apoptosis, despite the presence of IFN- β in supernatants (indicative of cGAS activation), no discernible change in the pattern of cGAS staining was apparent (fig. S6, A and B).

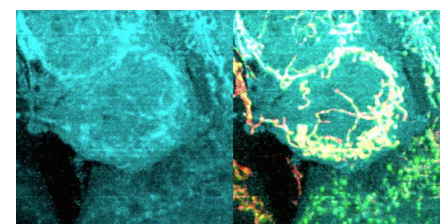
Given that cGAS did not appear within intact hernias or accumulate at their surface, we postulated that a loss of IMM integrity might facilitate mtDNA access to cGAS or vice versa. We

used correlative light and electron microscopy (CLEM) to enable the overlay of fluorescent signals and mitochondrial ultrastructure. *Mcl1*^{-/-} MEFs expressing TOMM20-Halo and TFAM-mNeonGreen were fixed 90 min after ABT-737 and QVD-OPh treatment, a time at which the majority of mitochondria had undergone herniation. These cells were subjected to confocal and electron microscopy, and the two images were correlated after acquisition (Fig. 6, A and B, and fig. S6D). Consistent with our immunogold TEM

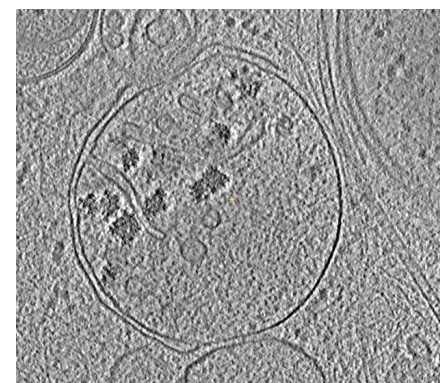
and ECT studies (Fig. 5, C to E, and fig. S6C), we observed many instances where the OMM had dissipated, with TFAM staining aligning to the IMM-bound structures (Fig. 6C). CLEM revealed instances where IMM integrity had been lost (Fig. 6, D and E, black arrows), although this was in a minority of mitochondrial hernias. The fact that this was in the minority of mitochondria is in line with the limited translocation of TFAM to the cytosolic fraction of apoptotic cells that we had observed by immunoblot (Fig. 2F). In rare cases, TFAM-positive, single membrane-bound structures were observed, some in close proximity to herniated mitochondria (Fig. 6E, red arrow) and some apparently isolated (Fig. 6F, red arrow).

Discussion

We have shown that BAK/BAX activation initiates a series of events that culminate in mtDNA release. Breakdown of the mitochondrial network follows BAK/BAX-mediated MOMP and cytochrome c efflux, and coincides with the formation of BAK/BAX foci large enough to be detected by LLSM. These BAK/BAX macropores allow the tightly packed IMM an outlet through which it herniates, carrying with it mitochondrial matrix components, including the mitochondrial genome. Although the elegant nature of the herniation event initially suggested a highly regulated process, we postulate that it is



Movie 7. Lattice light-sheet imaging of mitochondria (red, TOMM20-Halo), mtDNA (green, TFAM-mNeonGreen), and BAX (blue) from *Mcl1*^{-/-} *Bak*^{-/-} *Bax*^{-/-} MEFs overexpressing BAX-mRuby2 and undergoing apoptosis induced by ABT-737 and QVD-OPh. Images were captured at a rate of one 3D volume every 13 s.



Movie 8. Reconstructed cryo-tomogram of an apoptotic herniating mitochondria (from Fig. 5E) moving through the z axis.

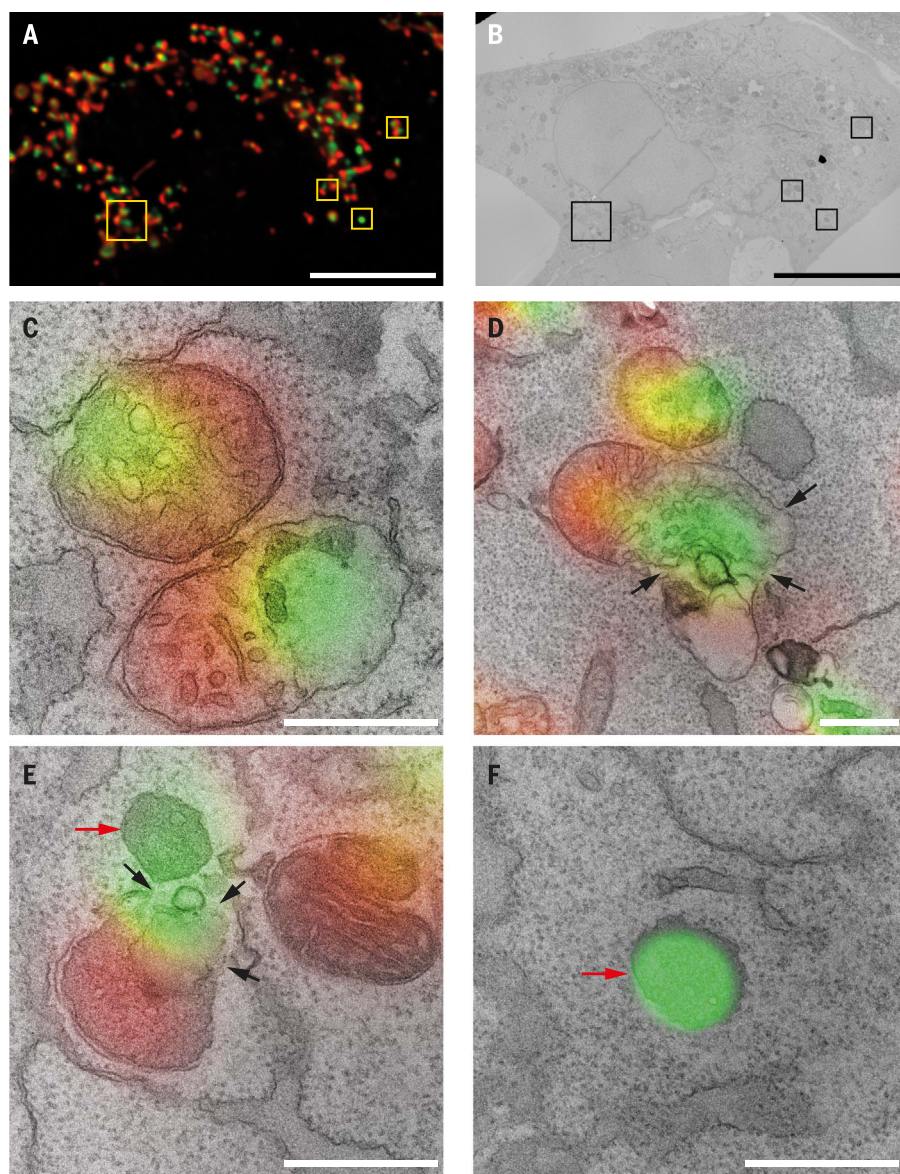


Fig. 6. Correlative light and electron microscopy of apoptotic mitochondrial herniation. (A) Confocal light microscopy imaging of *Mcl1*^{-/-} MEFs expressing TOMM20-Halo (stained with JF-546) (red) and TFAM-mNeonGreen (green), fixed 90 min after ABT-737 (1 μ M) + QVD-OPh (20 μ M) treatment. (B) TEM imaging of the same cells as in (A). Scale bars, 10 μ m. (C to F) Selected examples from (A) and (B) at higher resolution, displaying a light microscopy image overlaid on an aligned electron microscopy image. The example shown in (C) is representative of the majority of herniation events observed; those in (D) and (E), where there is evidence of IMM breakdown, were less frequent. The image in (F) is representative of the few observed examples of TFAM-positive, single-membrane walled structures. Scale bars, 500 nm.

simply the physical result of massive holes forming in the mitochondrial outer membrane (i.e., collateral damage). Upon exposure to the cytoplasm, IMM hernias lose integrity, facilitating the recognition of mtDNA by cGAS. Dissipation of the IMM appears to occur in a limited number of mitochondria, but enough mtDNA reaches the cytosol to initiate a robust cGAS/STING pathway response. This is consistent with recent reports highlighting the profound sensitivity of cGAS to cytosolic TFAM-bound DNA (64).

The requirement for mitochondrial fission in apoptotic cell death is controversial. Several studies suggest that it is essential, because DRP1 inhibition or deletion reportedly delays cytochrome c release and cell death [reviewed in (45, 65)]. In contrast, others have concluded that because DRP1 inhibition does not confer a level of protection equivalent to that of BCL-X_L overexpression, fission and mitochondrial apoptosis are independent processes (66). Our data support the latter view. The absence of DRP1 resulted in mitochondrial network hyperfusion in both the original knockout mouse-derived MEFs and the newly generated CRISPR-targeted clones, but it did not inhibit apoptotic mitochondrial network breakdown and herniation in the CRISPR lines. We suggest that, given the profound OMM damage induced by BAK and BAX, apoptotic breakdown is not a facsimile of normal mitochondrial fission. Recent work indicates that the endoplasmic reticulum contacts mitochondria near nucleoids engaged in replication, thereby marking points of mitochondrial division (67, 68). It will be interesting to see how these mechanisms might influence mitochondrial collapse during apoptosis. Even though the impairment of mitochondrial network breakdown that was apparent during apoptosis in the *Drp1* knockout MEF cell line is likely artifactual, this system does suggest that in any setting where fragmentation is compromised, the frequency of mitochondrial herniation events will be correspondingly reduced.

Our work provides a mechanistic description of mtDNA release from mitochondria during apoptosis. It occurs irrespective of caspase activity, but in normal cells, caspases attenuate the subsequent cGAS/STING-mediated antiviral response by driving rapid cellular collapse and clearance. Previous reports have shown that genetic ablation of the apoptotic caspase cascade in vivo—at least in the hematopoietic system—results in mtDNA-dependent IFN production (6, 7). We thus contend that IMM herniation is a common event in normal physiology and that it occurs in any cell whose homeostatic turnover is governed by BAK and BAX. An extensive literature suggests that mtDNA is found outside the mitochondria—and, indeed, outside the cell—in a wide range of circumstances (13, 69). This raises the question of whether BAK/BAX-mediated mtDNA release represents a source of circulating mtDNA at steady state, or in any of the conditions where increased levels of extracellular mtDNA have been implicated in disease pathology.

It is unclear whether IMM herniation represents a general mechanism of mtDNA escape.

In addition to BAK and BAX oligomerization there may be alternative triggers, for example, other pore-forming proteins (host- or pathogen-derived) or mitochondrial stresses. Indeed, whether and how herniation may be triggered during HIV or dengue infection, calcium overload, irradiation, or during inflammatory diseases such as systemic lupus erythematosus or rheumatoid arthritis—all conditions that have been associated with loss of mtDNA from the matrix (13, 69, 70)—remains to be established. In some of these conditions cytoplasmic mtDNA is thought to be the pathological trigger, while in others, it is extracellular mtDNA. Our findings demonstrate that herniation is one route to the former. It may, in some circumstances, also contribute to generation of the latter (fig. S6E). The TFAM-positive single membrane bound structures observed in the cytoplasm of apoptotic cells suggest that hernias may bud off, and as such, represent an additional class of mitochondrial-derived vesicles (71).

Materials and methods

Cell culture

MEFs were derived from mice on a C57BL/6 background or backcrossed for more than 10 generations and prepared from embryonic day 13–14 embryos. After removal of the head, thoracic cavity, and fetal liver, a single-cell suspension was prepared in Dulbecco's modified Eagle's (DME) medium (GIBCO, ThermoFisher 11965092) supplemented with 4 mM L-glutamine, glucose (4.5 g/liter), and 10% heat-inactivated fetal bovine serum (FBS; Sigma 12003C) and cultured at 37°C, 5% CO₂ on tissue culture plates coated with 0.1% gelatin. immortalization of MEFs was performed by transfection (Amara Nucleofector) of an expression plasmid encoding the SV40 T antigen (gift from D. C. S. Huang). immortalized MEF lines were routinely maintained at 37°C, 5% CO₂ in DME-KELSO medium [prepared in-house from DMEM (GIBCO 31600083) supplemented with 40 mM sodium bicarbonate, 1 mM HEPES, 0.0135 mM folic acid, 0.24 mM L-asparagine, 0.55 mM L-arginine, 1× Pen/Strep, and 22.2 mM D-glucose] supplemented with 10% heat-inactivated FBS, penicillin/streptomycin (Pen/Strep) (Sigma P0781, 10 µl/ml), and 100 µM L-asparagine (Sigma A4159). HeLa cells were maintained at 37°C, 5% CO₂ in DME medium supplemented with 10% heat-inactivated FBS and Pen/Strep. mtDNA depletion and assessment of mtDNA content was carried out as described (6). *Drp1*^{−/−}, *Opa1*^{−/−}, and *Mfn1*^{−/−} *Mfn2*^{−/−} MEF lines were a gift from M. Ryan. To generate knockout MEFs, we used transient CRISPR/Cas9-mediated gene targeting. Targeting guide sequences were designed using Benchling software, cloned into the px458 vector (containing Cas9 and GFP marker) [gift from F. Zhang (72): Addgene plasmid 48138] and were transfected into MEFs using Fugene 6 (Roche) at a 3:1 ratio. GFP-positive cells were sorted by flow cytometry (Influx) and clones derived from single cells were expanded. The targeted gene locus was sequenced and clones bearing indels predicted to disrupt gene function on both alleles were selected for further ex-

perimentation. Additionally, *Mcl1*^{CRISPR/−/−} clones were functionally tested by assessing their sensitivity to ABT-737 and immunoblotted for protein expression. *Drp1*^{CRISPR/−/−} clones were generated as described (72) on a *Mcl1*^{−/−} *Bax*^{−/−} background, reexpressing fluorescently tagged BAX, and clones were selected based on mitochondrial and peroxisomal morphology (assessed by confocal imaging) and immunoblot of protein expression. The targeting guide sequences were as follows: *Mcl1*#1, GATCATCTCGCGTACTTGC; *Mcl1*#2, GGAGCAGCGCACCGGCTCCA; cGAS#1, GATTCTTG-TAGCTCAATCCTG; cGAS#2, GAAATCAAAAGA-ATTCCACG; *Drp1*, GCAGGACGTCTTCAACACAG.

Constructs and reagents

Imaging constructs were generated using PCR amplification of sequences encoding the fluorescent proteins mNeonGreen (Allele Biotechnology), pBabe (LTR)-cytochrome c-GFP [gift from D. Green (25): Addgene plasmid 41183], pTRIP-CMV-GFP-FLAG-cGAS [gift from N. Manel (73): Addgene plasmid 86675], mRuby2-NT-C1 [gift from M. Davidson (74): Addgene plasmid 54561], pCytERM-mScarlet-N1 [gift from D. Gadella (75): Addgene plasmid 85066] mCherry, tdTomato (gift from D. C. S. Huang), or the HaloTag (Promega). These were cloned into an MSCV-IRES-hygromycin or MSCV-IRES-puromycin construct (a hygromycin/puromycin selectable retroviral vector) such that they were fused either N-terminally to BAK or BAX (murine coding sequences, gifts from D. Huang) or C-terminally to the matrix targeting sequence from OTC, DMAC1 (gift from M. Ryan), TFAM (OriGene NM_009360), or TOMM20 (GenScript synthesis NM_014765.2) sequences. MEF lines stably expressing fluorescent fusion proteins were prepared as follows: Expression plasmids were transiently transfected into Phoenix ecotropic packaging cells using Eugene 6 (Roche). Viral supernatants were collected 48 hours later and used to infect MEFs by spin infection. Cell populations expressing the fluorescent fusion proteins were sorted by flow cytometry (Influx). Drug treatments used throughout the study include QVD-OPH (MedKoo Biosciences 1135695-98-5, MP Biomedicals 03OPH109, or made in-house by R. Lessene), ABT-737 (Active Biochemicals A-1002), S63845 (SYNthesis MedChem), cyclosporin A (Sigma 30024), antimycin A (Sigma A8674, CAS:1397-94-0), and oligomycin A (Selleck S1478, CAS:579-13-5).

Viability assay

Cell viability was quantified by CellTiterGlo (Promega G7570) or flow cytometric analysis of cells excluding propidium iodide (Sigma P4864, 5 µg/ml).

ELISA

IFN-β protein was measured using the VeriKine-HS Mouse Interferon Beta ELISA (PBL Assay Science 42410) as per manufacturer's instructions.

Subcellular fractionation and immunoblotting

Cells were grown overnight in 10-cm dishes, pretreated with QVD-OPH (50 µM) for 30 min,

then treated with ABT-737 (1 μ M) for times as indicated. Culture supernatants were retrieved for analysis of IFN- β by ELISA, and cells were trypsinized and fractionated into cytosol and mitochondria-enriched heavy membrane fractions by incubating in 0.025% w/v digitonin (Biosynth) in 20 mM Hepes KOH pH 7.5, 93 mM sucrose, 100 mM KCl, 2.5 mM $MgCl_2$ for 10 min on ice. Cytosol and heavy membrane fractions were separated by centrifugation at 13,000g for 5 min at 4°C, before analysis on reducing SDS-PAGE, transfer to nitrocellulose membrane, and immunoblotting for TFAM (ab131607, Abcam), cytochrome c (556433, BD Biosciences), DLD [sc-365977 (G-2), Santa Cruz Biotechnologies], and VDAC1 (MABN504, Merck).

Confocal microscopy

For imaging of cells at steady state, cells were plated in 8-well chamber slides (iBidi 80826) and incubated with PicoGreen dye (InvivoGen, 3 μ l/ml) in serum-free medium for 1 hour at 37°C, and Mitotracker Red-FM dye (InvivoGen, 1 μ M) for 30 min (added halfway through PicoGreen staining). For imaging of apoptotic cells, cells were plated in 8-well chamber slides (iBidi 80826) and incubated with drug treatments at 37°C for indicated times, after which media was replaced with 2% paraformaldehyde (Electron Microscopy Sciences 15710). Cells were left to fix for 15 min, before three washes in phosphate-buffered saline (PBS), and incubated at room temperature for 40 min in permeabilization/blocking buffer of 0.1% Tween (Sigma P1379), 3% goat serum (Life Technologies 501972). Cells were then incubated overnight at 4°C with primary antibodies anti-TOMM20 (Santa Cruz Biotech sc-11415) and anti-DNA (ProGen AC-30-10) in blocking buffer, washed twice, then incubated for 1 hour in secondary antibodies [goat anti-rabbit AF647 (Life Technologies A21245) and goat anti-mouse AF488 (Life Technologies A11001)]. In both cases, wells were then washed in PBS, before phenol red-free medium was added and cells imaged on the Zeiss LSM 780 confocal microscope using a 63 \times /1.4 Plan Apo objective. Images shown are maximum-intensity projections from Z-stacks.

Lattice light-sheet microscopy

The lattice light-sheet microscopes used in these experiments are housed in the Advanced Imaging Center (AIC) at the Howard Hughes Medical Institute Janelia Research Campus, or the Walter & Eliza Hall Institute of Medical Research. The systems were configured and operated as described (14). For all experiments, MEFs were grown on 5-mm round glass coverslips (Warner Instruments CS-5R). All drug treatments were done after sample mounting in the imaging/media chamber, with the exception of PicoGreen (Invitrogen, ThermoFisher P7581) or TMRM (Sigma T5428) staining and CsA pretreatments, which were done 30 min before sample mounting. During imaging, cells were maintained in Leibovitz's L-15 medium (GIBCO, ThermoFisher 21083027) supplemented with 10% FBS, 25 mM HEPES (GIBCO, ThermoFisher 15630080), Pen/Strep

(Sigma P0781, 10 μ l/ml), 100 μ M L-asparagine (Sigma A4159), and 20 μ M TROLOX (Santa Cruz 53188-07-1). Samples were illuminated by lattice light-sheet using 488-nm, 560-nm, or 641-nm diode lasers (MPB Communications) through an excitation objective (Special Optics, 0.65 NA, 3.74-mm WD) at 70 to 75%, 40 to 80%, and 60 to 100% AOTF transmittance (respectively) and 90 mW, 75 mW, and 100 mW initial box power (respectively) for the Janelia system, or 10 to 25%, 15 to 35%, and 10 to 25% AOTF transmittance (respectively) and 30 to 60 mW, 50 to 100 mW, and 50 to 100 mW initial box power (respectively) for the WEHI system. The lattice light-sheet was illuminated at the back aperture of the excitation objective through an annular mask of 0.44 inner NA and 0.55 outer NA. Fluorescent emission was collected by detection objective (Nikon, CFI Apo LWD 25XW, 1.1 NA) and detected by sCMOS cameras (Hamamatsu Orca Flash 4.0 v2). Acquired data were deskewed as described (14) and deconvolved using an iterative Richardson-Lucy algorithm. Point-spread functions for deconvolution were experimentally measured using 200-nm TetraSpeck beads adhered to 5-mm glass coverslips (Invitrogen T7280) for each excitation wavelength.

Live 3D structure illumination microscopy

Live, two-color, 3D-SIM images were captured on a custom-built structured illumination microscope housed in the Advanced Imaging Center (AIC) at the Howard Hughes Medical Institute, Janelia Research Campus. This platform consists of a Zeiss AxioObserver inverted microscope platform with a motorized stage and Zeiss 100 \times /1.46 NA oil immersion objective. Laser excitation was achieved with 488-nm and 561-nm lasers using an acousto-optical modulator, which is synchronized with a spatial light modulator for fast dual color switching at each optical plane as described (76). Cells were maintained at 37°C, 5% CO₂ in Leibovitz's L-15 medium (GIBCO, ThermoFisher 21083027) supplemented with 10% FBS, 25 mM HEPES (GIBCO, ThermoFisher 15630080), Pen/Strep (Sigma P0781, 10 μ l/ml), 100 μ M L-asparagine (Sigma A4159), and 20 μ M TROLOX (Santa Cruz 53188-07-1). All drug treatments were done after sample mounting in the imaging/media chamber. 512 \times 512 images of each channel were collected serially on two separate sCMOS cameras (Hamamatsu Flash 4.0) and camera exposures were typically set at 10 or 20 ms. The step size was set at 150 nm, and z-thicknesses of 1.35 to 2.85 μ m were captured at each time point. The reconstruction of the data was performed using a custom-written program and all chromatic alignments were performed after acquisition.

Live, three-color, 3D-SIM imaging was performed on the OMX-SR system (GE Healthcare). This platform consists of an Olympus 60 \times 1.42 NA oil immersion lens and three PCO.edge sCMOS cameras. Laser excitation was achieved with 488-nm, 561-nm, and 642-nm lasers. During imaging, cells were maintained at 25°C, 5% CO₂ in Fluorobrite DMEM medium (GIBCO, ThermoFisher A1896701) supplemented with 10% FBS, 25 mM

HEPES (GIBCO, ThermoFisher 15630080), Pen/Strep (Sigma P0781, 10 μ l/ml), 100 μ M L-asparagine (Sigma A4159) and 20 μ M TROLOX (Santa Cruz 53188-07-1). 512 \times 512 images were captured with camera exposures kept below 10 ms. The step size was set at 125 nm, and volumes varied between 1.0 and 2.5 μ m for each time point. The reconstruction and chromatic alignment of data was performed using SoftWorx (GE Healthcare) with a Wiener filter set at 0.005. For all experiments, MEFs were grown on 23-mm round glass coverslips (Warner Instruments). All SIM data, including raw and reconstructed images, were subjected to SIMcheck FIJI Plugin (77) to ensure that image quality was within acceptable standards.

Immunogold transmission electron microscopy

Fixation and embedding procedures were carried out as described (78). Sections were cut on a Leica FC7-UC7. Immunolabeling was done with goat anti-GFP/biotin (Rockland 600-106-215) and rabbit anti-biotin (Rockland, 100-4198) followed by incubation with protein-A-Gold 15 nm (Department of Cell Biology, University Medical Center, Utrecht). High-resolution EM images were taken on a Hitachi H-7500 TEM and a FEI Tecnai T12 TEM.

Correlative light and electron microscopy

Mcl1^{-/-} MEFs expressing TOMM20-Halo and TFAM-mNeonGreen were grown overnight in a 35 mm 500-grid plastic-bottomed μ -Dish (Ibidi, Germany). After treatment with QVD-Oph (20 μ M) and ABT-737 (1 μ M), cells were stained with CellMask Deep Red Plasma Membrane stain (ThermoFisher, 2.5 μ g/ml) and JaneliaFluor-646 HaloTag-specific dye (17) (50 nm) for 30 min at 37°C and 5% CO₂, then fixed using prewarmed phosphate-buffered 4% paraformaldehyde at 37°C for 1 hour. The fixed sample was imaged on an inverted Leica SP8 confocal laser scanning microscope equipped with an 40 \times /1.10 objective (water immersion, HC PLAPO, CS2; Leica microsystems) using an HyD Hybrid Detector (Leica Biosystems) through the Leica Application Suite X (LASX v2.0.1). The optical data (35 nm lateral pixel resolution; 200 nm axial voxel resolution) was deconvolved for subsequent alignment (fast classic maximum likelihood estimation; 10 signal-to-noise ratio; 40 iterations; 0.05 quality threshold) using Huygens Professional (v15.10; Scientific Volume Imaging). After optical image acquisition, the sample was post-fixed overnight with 2.5% glutaraldehyde in 0.1 M sodium cacodylate buffer at 4°C, rinsed twice with 0.1 M sodium cacodylate, then osmicated with ferricyanide-reduced osmium tetroxide (1% (w/v) OsO₄, 1.5% (w/v) K₂[Fe(CN)₆], 0.065 M cacodylate buffer) for 2 hours at 4°C, and thoroughly rinsed five times using MilliQ water. All subsequent stages were microwave assisted using a BioWave Pro microwave system (Pelco). The sample was en bloc stained with 2% (w/v) aqueous uranyl acetate using three microwave duty cycles (120 s on, 120 s off) at 100 W under vacuum, then rinsed five times with MilliQ water. Microwave-assisted

dehydration was performed at atmospheric pressure using 150 W for 40 s per stage of a graduated series of ethanol (50%, 70%, 90%, 100%, 100%) and propylene oxide (100%, 100%), and microwave-assisted resin infiltration was performed under vacuum at 250 W for 180 s per stage using a graduated series of Procure-Araldite (25%, 50%, 75%, 100%, 100%) in propylene oxide, before resin polymerization at 60°C for 48 hours. The target depth within the target cell was then relocated within the resin block, using the procedure outlined in (79). The resin block was trimmed, then sectioned using Ultracut UCT ultramicrotome (Leica) equipped with a 45° diamond knife (Diatome) to cut serial sections (average thickness 78 nm) for collection on nine separate 300-mesh hex thin-bar copper grids. Grids containing the sections closest to the target z-planes (1000 nm to 1600 nm depth into resin block) were stained at room temperature using 2% (w/v) aqueous uranyl acetate (10 min) and Reynolds lead citrate (3 min). A 27-image TEM montage of the target cell was manually acquired using a Tecnai T12 TEM operated at 120 kV. The image montage was corrected for EM lens distortion and stitched by linear blending using the appropriate plugins in FIJI (FIJI Is Just ImageJ) (27, 80, 87). Within GIMP (GNU Image Manipulation Program, version 2.8.2), the distortion-corrected TEM montage was aligned with the deconvolved optical data using filopodia, the nucleus, and other intrinsic features as anchor points. All subsequent TEM data were aligned directly to this canonical alignment. Correlated fluorescence data were obtained by scaling and aligning TEM images to the TEM montage, extracting the aligned region from the fluorescence channels, then performing the reverse operations with bicubic interpolation.

Electron cryotomography

Cells were grown overnight on 200 mesh Quantifoil gold grids, stimulated for 90 min with ABT-737 (1 μ M) + QVD-OPh (20 μ M), and cryo-fixed in liquid ethane using a Vitrobot Mark IV. Continuous cryo-tomograms from -60° to 60° were recorded on a Titan Krios at a magnification of 19,500 using the Volta phase plate, an energy filter, and a K2 Summit camera at a dose of about 90 electrons per angstrom. Reconstruction was done using the IMOD Tomography package. Tomographic slices of 10-nm thickness are shown.

Data analysis

All image data were analyzed using the FIJI distribution of ImageJ (27). The segmentation of mitochondria and TFAM signal was performed using the WEKA Trainable Segmentation plugin. Segmentation was trained on representative frames of five images from different data sets, then applied to all frames of all data sets. All resultant segmentation was then also validated visually. Mitochondrial morphology was measured using FIJI's in-built morphology measures. Cytochrome c release was measured by calculating the area (pixels) of signal above background, within the segmented mitochondria signal, which was set manually at a level that was consistent

between all data sets and accurately matched the behavior that was qualitatively observed. This was then graphed relative to mitochondrial area (i.e., cytochrome c area/mito area) to ensure that changes in cytochrome c area were not artifacts of changing mitochondrial morphology. For nucleoid release measurements, the TFAM signal was segmented, thresholded, and masked with the inverse of the segmented mitochondria signal, thereby ensuring that only signal from TFAM outside the mitochondria would be measured. BAX aggregation was quantified by segmenting and counting all regions of BAX signal above a set size and intensity limit as they appeared over time. For all manual adjustments, threshold values were set using representative frames and validated against additional frames (from later time points) before application to the entire time course. Once threshold values had been set and validated, all measurements were then automated across all independent experiments and time points.

Code availability

Custom scripts automating the combinations of FIJI in-built plugins/filters used for analysis are available as supplementary files (code files S1 and S2).

REFERENCES AND NOTES

1. R. J. Youle, A. Strasser, The BCL-2 protein family: Opposing activities that mediate cell death. *Nat. Rev. Mol. Cell Biol.* **9**, 47–59 (2008). doi: [10.1038/nrm2308](https://doi.org/10.1038/nrm2308); pmid: [18097445](https://pubmed.ncbi.nlm.nih.gov/18097445/)
2. P. E. Czabotar, G. Lessene, A. Strasser, J. M. Adams, Control of apoptosis by the BCL-2 protein family: Implications for physiology and therapy. *Nat. Rev. Mol. Cell Biol.* **15**, 49–63 (2014). doi: [10.1038/nrm3722](https://doi.org/10.1038/nrm3722); pmid: [24355989](https://pubmed.ncbi.nlm.nih.gov/24355989/)
3. R. M. Kluck, E. Bossy-Wetzel, D. R. Green, D. D. Newmeyer, The release of cytochrome c from mitochondria: A primary site for Bcl-2 regulation of apoptosis. *Science* **275**, 1132–1136 (1997). doi: [10.1126/science.275.5303.1132](https://doi.org/10.1126/science.275.5303.1132); pmid: [9027315](https://pubmed.ncbi.nlm.nih.gov/9027315/)
4. J. Yang et al., Prevention of apoptosis by Bcl-2: Release of cytochrome c from mitochondria blocked. *Science* **275**, 1129–1132 (1997). doi: [10.1126/science.275.5303.1129](https://doi.org/10.1126/science.275.5303.1129); pmid: [9027314](https://pubmed.ncbi.nlm.nih.gov/9027314/)
5. O. Julien, J. A. Wells, Caspases and their substrates. *Cell Death Differ.* **24**, 1380–1389 (2017). doi: [10.1038/cdd.2017.44](https://doi.org/10.1038/cdd.2017.44); pmid: [28498362](https://pubmed.ncbi.nlm.nih.gov/28498362/)
6. M. J. White et al., Apoptotic caspases suppress mtDNA-induced STING-mediated type I IFN production. *Cell* **159**, 1549–1562 (2014). doi: [10.1016/j.cell.2014.11.036](https://doi.org/10.1016/j.cell.2014.11.036); pmid: [25525874](https://pubmed.ncbi.nlm.nih.gov/25525874/)
7. A. Rongvaux et al., Apoptotic caspases prevent the induction of type I interferons by mitochondrial DNA. *Cell* **159**, 1563–1577 (2014). doi: [10.1016/j.cell.2014.11.037](https://doi.org/10.1016/j.cell.2014.11.037); pmid: [25525875](https://pubmed.ncbi.nlm.nih.gov/25525875/)
8. M. Patrushev et al., Mitochondrial permeability transition triggers the release of mtDNA fragments. *Cell. Mol. Life Sci.* **61**, 3100–3103 (2004). doi: [10.1007/s00108-004-4424-1](https://doi.org/10.1007/s00108-004-4424-1); pmid: [15583871](https://pubmed.ncbi.nlm.nih.gov/15583871/)
9. M. Patrushev et al., Release of mitochondrial DNA fragments from brain mitochondria of irradiated mice. *Mitochondrion* **6**, 43–47 (2006). doi: [10.1016/j.mito.2005.12.001](https://doi.org/10.1016/j.mito.2005.12.001); pmid: [16413832](https://pubmed.ncbi.nlm.nih.gov/16413832/)
10. A. P. West et al., Mitochondrial DNA stress primes the antiviral innate immune response. *Nature* **520**, 553–557 (2015). doi: [10.1038/nature14156](https://doi.org/10.1038/nature14156); pmid: [25642965](https://pubmed.ncbi.nlm.nih.gov/25642965/)
11. K. Shimada et al., Oxidized mitochondrial DNA activates the NLRP3 inflammasome during apoptosis. *Immunity* **36**, 401–414 (2012). doi: [10.1016/j.immuni.2012.01.009](https://doi.org/10.1016/j.immuni.2012.01.009); pmid: [22342844](https://pubmed.ncbi.nlm.nih.gov/22342844/)
12. T.-D. Kanneganti, M. Kundu, D. R. Green, Innate immune recognition of mtDNA—an undercover signal? *Cell Metab.* **21**, 793–794 (2015). doi: [10.1016/j.cmet.2015.05.019](https://doi.org/10.1016/j.cmet.2015.05.019); pmid: [26039443](https://pubmed.ncbi.nlm.nih.gov/26039443/)
13. A. P. West, G. S. Shadel, Mitochondrial DNA in innate immune responses and inflammatory pathology. *Nat. Rev. Immunol.* **17**, 363–375 (2017). doi: [10.1038/nri.2017.21](https://doi.org/10.1038/nri.2017.21); pmid: [28393922](https://pubmed.ncbi.nlm.nih.gov/28393922/)
14. B.-C. Chen et al., Lattice light-sheet microscopy: Imaging molecules to embryos at high spatiotemporal resolution. *Science* **346**, 1257998–1257998 (2014). doi: [10.1126/science.1257998](https://doi.org/10.1126/science.1257998); pmid: [25342811](https://pubmed.ncbi.nlm.nih.gov/25342811/)
15. T. Oltersdorf et al., An inhibitor of Bcl-2 family proteins induces regression of solid tumours. *Nature* **435**, 677–681 (2005). doi: [10.1038/nature03579](https://doi.org/10.1038/nature03579); pmid: [15902208](https://pubmed.ncbi.nlm.nih.gov/15902208/)
16. M. F. van Delft et al., The BH3 mimetic ABT-737 targets selective Bcl-2 proteins and efficiently induces apoptosis via Bak/Bax if Mcl-1 is neutralized. *Cancer Cell* **10**, 389–399 (2006). doi: [10.1016/j.ccr.2006.08.027](https://doi.org/10.1016/j.ccr.2006.08.027); pmid: [17097561](https://pubmed.ncbi.nlm.nih.gov/17097561/)
17. J. B. Grimm et al., A general method to improve fluorophores for live-cell and single-molecule microscopy. *Nat. Methods* **12**, 244–250 (2015). doi: [10.1016/j.ccr.2006.08.027](https://doi.org/10.1016/j.ccr.2006.08.027); pmid: [17097561](https://pubmed.ncbi.nlm.nih.gov/17097561/)
18. N. C. Shaner et al., A bright monomeric green fluorescent protein derived from *Branchiostoma lanceolatum*. *Nat. Methods* **10**, 407–409 (2013). doi: [10.1038/nmeth.2413](https://doi.org/10.1038/nmeth.2413); pmid: [23524392](https://pubmed.ncbi.nlm.nih.gov/23524392/)
19. T. M. Caserta, A. N. Smith, A. D. Gultice, M. A. Reedy, T. L. Brown, Q-VD-OPh, a broad spectrum caspase inhibitor with potent antiapoptotic properties. *Apoptosis* **8**, 345–352 (2003). doi: [10.1023/A:1024116916932](https://doi.org/10.1023/A:1024116916932); pmid: [12815277](https://pubmed.ncbi.nlm.nih.gov/12815277/)
20. A. Kotschy et al., The MCL1 inhibitor S63845 is tolerable and effective in diverse cancer models. *Nature* **538**, 477–482 (2016). doi: [10.1038/nature19830](https://doi.org/10.1038/nature19830); pmid: [27760111](https://pubmed.ncbi.nlm.nih.gov/27760111/)
21. N. Ashley, D. Harris, J. Poulton, Detection of mitochondrial DNA depletion in living human cells using PicoGreen staining. *Exp. Cell Res.* **303**, 432–446 (2005). doi: [10.1016/j.yexcr.2004.10.013](https://doi.org/10.1016/j.yexcr.2004.10.013); pmid: [15652355](https://pubmed.ncbi.nlm.nih.gov/15652355/)
22. P. D. Bhola, A. L. Mattheyses, S. M. Simon, Spatial and temporal dynamics of mitochondrial membrane permeability waves during apoptosis. *Biophys. J.* **97**, 2222–2231 (2009). doi: [10.1016/j.bpj.2009.07.056](https://doi.org/10.1016/j.bpj.2009.07.056); pmid: [19843454](https://pubmed.ncbi.nlm.nih.gov/19843454/)
23. M. Rehm et al., Dynamics of outer mitochondrial membrane permeabilization during apoptosis. *Cell Death Differ.* **16**, 613–623 (2009). doi: [10.1038/cdd.2008.187](https://doi.org/10.1038/cdd.2008.187); pmid: [19136937](https://pubmed.ncbi.nlm.nih.gov/19136937/)
24. M. Rehm, H. Düsselmann, J. H. M. Prehn, Real-time single cell analysis of Smac/DIABLO release during apoptosis. *J. Cell Biol.* **162**, 1031–1043 (2003). doi: [10.1083/jcb.200303123](https://doi.org/10.1083/jcb.200303123); pmid: [12975347](https://pubmed.ncbi.nlm.nih.gov/12975347/)
25. J. C. Goldstein, N. J. Waterhouse, P. Juin, G. I. Evan, D. R. Green, The coordinate release of cytochrome c during apoptosis is rapid, complete and kinetically invariant. *Nat. Cell Biol.* **2**, 156–162 (2000). doi: [10.1038/35004029](https://doi.org/10.1038/35004029); pmid: [10707086](https://pubmed.ncbi.nlm.nih.gov/10707086/)
26. L. Lartigue et al., An intracellular wave of cytochrome c propagates and precedes Bax redistribution during apoptosis. *J. Cell Sci.* **121**, 3515–3523 (2008). doi: [10.1242/jcs.029587](https://doi.org/10.1242/jcs.029587); pmid: [18840646](https://pubmed.ncbi.nlm.nih.gov/18840646/)
27. J. Schindelin et al., Fiji: An open-source platform for biological-image analysis. *Nat. Methods* **9**, 676–682 (2012). doi: [10.1038/nmeth.2019](https://doi.org/10.1038/nmeth.2019); pmid: [22743772](https://pubmed.ncbi.nlm.nih.gov/22743772/)
28. B. Westermann, Mitochondrial fusion and fission in cell life and death. *Nat. Rev. Mol. Cell Biol.* **11**, 872–884 (2010). doi: [10.1038/nrm3013](https://doi.org/10.1038/nrm3013); pmid: [21102612](https://pubmed.ncbi.nlm.nih.gov/21102612/)
29. R. J. Youle, A. M. van der Bliek, Mitochondrial fission, fusion, and stress. *Science* **337**, 1062–1065 (2012). doi: [10.1126/science.1219855](https://doi.org/10.1126/science.1219855); pmid: [22936770](https://pubmed.ncbi.nlm.nih.gov/22936770/)
30. L. Pernas, L. Scorrano, Mito-morphosis: Mitochondrial fusion, fission, and cristae remodeling as key mediators of cellular function. *Annu. Rev. Physiol.* **78**, 505–531 (2016). doi: [10.1146/annurev-physiol-021115-105011](https://doi.org/10.1146/annurev-physiol-021115-105011); pmid: [26667075](https://pubmed.ncbi.nlm.nih.gov/26667075/)
31. J. R. Friedman, J. Nunnari, Mitochondrial form and function. *Nature* **505**, 335–343 (2014). doi: [10.1038/nature12985](https://doi.org/10.1038/nature12985); pmid: [24429632](https://pubmed.ncbi.nlm.nih.gov/24429632/)
32. E. Smirnova, L. Griparic, D. L. Shurland, A. M. van der Bliek, Dynamin-related protein Drp1 is required for mitochondrial division in mammalian cells. *Mol. Biol. Cell* **12**, 2245–2256 (2001). doi: [10.1091/mbc.12.8.2245](https://doi.org/10.1091/mbc.12.8.2245); pmid: [11514614](https://pubmed.ncbi.nlm.nih.gov/11514614/)
33. J. Prudent, H. M. McBride, Mitochondrial dynamics: ER actin tightens the Drp1 noose. *Curr. Biol.* **26**, R207–R209 (2016). doi: [10.1016/j.cub.2016.01.009](https://doi.org/10.1016/j.cub.2016.01.009); pmid: [26954442](https://pubmed.ncbi.nlm.nih.gov/26954442/)
34. N. Ishihara, Y. Eura, K. Mihara, Mitofusin 1 and 2 play distinct roles in mitochondrial fusion reactions via GTPase activity. *J. Cell Sci.* **117**, 6535–6546 (2004). doi: [10.1242/jcs.01565](https://doi.org/10.1242/jcs.01565); pmid: [15572413](https://pubmed.ncbi.nlm.nih.gov/15572413/)
35. S. Cipolat, O. Martins de Brito, B. Dal Zilio, L. Scorrano, OPA1 requires mitofusin 1 to promote mitochondrial fusion. *Proc. Natl. Acad. Sci. U.S.A.* **101**, 15927–15932 (2004). doi: [10.1073/pnas.0407043101](https://doi.org/10.1073/pnas.0407043101); pmid: [15509649](https://pubmed.ncbi.nlm.nih.gov/15509649/)
36. I. Martinou et al., The release of cytochrome c from mitochondria during apoptosis of NGF-deprived sympathetic neurons is a reversible event. *J. Cell Biol.* **144**, 883–889 (1999). doi: [10.1083/jcb.144.5.883](https://doi.org/10.1083/jcb.144.5.883); pmid: [10085288](https://pubmed.ncbi.nlm.nih.gov/10085288/)

37. S. Frank *et al.*, The role of dynamin-related protein 1, a mediator of mitochondrial fission, in apoptosis. *Dev. Cell* **1**, 515–525 (2001). doi: [10.1016/S1534-5807\(01\)00055-7](https://doi.org/10.1016/S1534-5807(01)00055-7); pmid: [11703942](https://pubmed.ncbi.nlm.nih.gov/11703942/)
38. M. Karbowski *et al.*, Quantitation of mitochondrial dynamics by photolabeling of individual organelles shows that mitochondrial fusion is blocked during the Bax activation phase of apoptosis. *J. Cell Biol.* **164**, 493–499 (2004). doi: [10.1083/jcb.200309082](https://doi.org/10.1083/jcb.200309082); pmid: [14769861](https://pubmed.ncbi.nlm.nih.gov/14769861/)
39. C. Sheridan, P. Delivani, S. P. Cullen, S. J. Martin, Bax- or Bak-induced mitochondrial fission can be uncoupled from cytochrome C release. *Mol. Cell* **31**, 570–585 (2008). doi: [10.1016/j.molcel.2008.08.002](https://doi.org/10.1016/j.molcel.2008.08.002); pmid: [18722181](https://pubmed.ncbi.nlm.nih.gov/18722181/)
40. M. Karbowski *et al.*, Spatial and temporal association of Bax with mitochondrial fission sites, Drp1, and Mfn2 during apoptosis. *J. Cell Biol.* **159**, 931–938 (2002). doi: [10.1083/jcb.200209124](https://doi.org/10.1083/jcb.200209124); pmid: [12499352](https://pubmed.ncbi.nlm.nih.gov/12499352/)
41. S. Wasiak, R. Zunino, H. M. McBride, Bax/Bak promote sumoylation of DRP1 and its stable association with mitochondria during apoptotic cell death. *J. Cell Biol.* **177**, 439–450 (2007). doi: [10.1083/jcb.200610042](https://doi.org/10.1083/jcb.200610042); pmid: [17470634](https://pubmed.ncbi.nlm.nih.gov/17470634/)
42. S. Montessuit *et al.*, Membrane remodeling induced by the dynamin-related protein Drp1 stimulates Bax oligomerization. *Cell* **142**, 889–901 (2010). doi: [10.1016/j.cell.2010.08.017](https://doi.org/10.1016/j.cell.2010.08.017); pmid: [20850011](https://pubmed.ncbi.nlm.nih.gov/20850011/)
43. H. Otera, N. Miyata, O. Kuge, K. Mihara, Drp1-dependent mitochondrial fission via Mif49/51 is essential for apoptotic cristae remodeling. *J. Cell Biol.* **212**, 531–544 (2016). doi: [10.1083/jcb.201508099](https://doi.org/10.1083/jcb.201508099); pmid: [26903540](https://pubmed.ncbi.nlm.nih.gov/26903540/)
44. D.-F. Suen, K. L. Norris, R. J. Youle, Mitochondrial dynamics and apoptosis. *Genes Dev.* **22**, 1577–1590 (2008). doi: [10.1101/gad.1658508](https://doi.org/10.1101/gad.1658508); pmid: [18559474](https://pubmed.ncbi.nlm.nih.gov/18559474/)
45. J. C. Martinou, R. J. Youle, Which came first, the cytochrome c release or the mitochondrial fission? *Cell Death Differ.* **13**, 1291–1295 (2006). doi: [10.1038/sj.cdd.4401985](https://doi.org/10.1038/sj.cdd.4401985); pmid: [16763618](https://pubmed.ncbi.nlm.nih.gov/16763618/)
46. L. A. Gillies, T. Kuwana, Apoptosis regulation at the mitochondrial outer membrane. *J. Cell. Biochem.* **115**, 632–640 (2014). doi: [10.1002/jcb.24709](https://doi.org/10.1002/jcb.24709); pmid: [24453042](https://pubmed.ncbi.nlm.nih.gov/24453042/)
47. B. Oettinghaus *et al.*, DRP1-dependent apoptotic mitochondrial fission occurs independently of BAX, BAK and APAF1 to amplify cell death by BID and oxidative stress. *Biochim. Biophys. Acta* **1857**, 1267–1276 (2016). doi: [10.1016/j.bbabi.2016.03.016](https://doi.org/10.1016/j.bbabi.2016.03.016); pmid: [26997499](https://pubmed.ncbi.nlm.nih.gov/26997499/)
48. A. Olichon *et al.*, Loss of OPA1 perturbs the mitochondrial inner membrane structure and integrity, leading to cytochrome c release and apoptosis. *J. Biol. Chem.* **278**, 7743–7746 (2003). doi: [10.1074/jbc.C200677200](https://doi.org/10.1074/jbc.C200677200); pmid: [12509422](https://pubmed.ncbi.nlm.nih.gov/12509422/)
49. R. Sugioka, S. Shimizu, Y. Tsujimoto, Fzo1, a protein involved in mitochondrial fusion, inhibits apoptosis. *J. Biol. Chem.* **279**, 52726–52734 (2004). doi: [10.1074/jbc.M408910200](https://doi.org/10.1074/jbc.M408910200); pmid: [15459195](https://pubmed.ncbi.nlm.nih.gov/15459195/)
50. D. Arnoult, A. Grodet, Y.-J. Lee, J. Estaquier, C. Blackstone, Release of OPA1 during apoptosis participates in the rapid and complete release of cytochrome c and subsequent mitochondrial fragmentation. *J. Biol. Chem.* **280**, 35742–35750 (2005). doi: [10.1074/jbc.M505970200](https://doi.org/10.1074/jbc.M505970200); pmid: [16115883](https://pubmed.ncbi.nlm.nih.gov/16115883/)
51. N. Ishihara *et al.*, Mitochondrial fission factor Drp1 is essential for embryonic development and synapse formation in mice. *Nat. Cell Biol.* **11**, 958–966 (2009). doi: [10.1038/ncb1907](https://doi.org/10.1038/ncb1907); pmid: [19578372](https://pubmed.ncbi.nlm.nih.gov/19578372/)
52. J. Wakabayashi *et al.*, The dynamin-related GTPase Drp1 is required for embryonic and brain development in mice. *J. Cell Biol.* **186**, 805–816 (2009). doi: [10.1083/jcb.200903065](https://doi.org/10.1083/jcb.200903065); pmid: [19752021](https://pubmed.ncbi.nlm.nih.gov/19752021/)
53. C. P. Baines *et al.*, Loss of cyclophilin D reveals a critical role for mitochondrial permeability transition in cell death. *Nature* **434**, 658–662 (2005). doi: [10.1038/nature03434](https://doi.org/10.1038/nature03434); pmid: [15800627](https://pubmed.ncbi.nlm.nih.gov/15800627/)
54. V. Petronilli, A. Nicoli, P. Costantini, R. Colonna, P. Bernardi, Regulation of the permeability transition pore, a voltage-dependent mitochondrial channel inhibited by cyclosporin A. *Biochim. Biophys. Acta* **1187**, 255–259 (1994). doi: [10.1016/0005-2728\(94\)90122-8](https://doi.org/10.1016/0005-2728(94)90122-8); pmid: [7521212](https://pubmed.ncbi.nlm.nih.gov/7521212/)
55. K. G. Wolter *et al.*, Movement of Bax from the cytosol to mitochondria during apoptosis. *J. Cell Biol.* **139**, 1281–1292 (1997). doi: [10.1083/jcb.139.5.1281](https://doi.org/10.1083/jcb.139.5.1281); pmid: [9382873](https://pubmed.ncbi.nlm.nih.gov/9382873/)
56. A. Neschutshan, C. L. Smith, I. Lamensdorf, S. H. Yoon, R. J. Youle, Bax and Bak coalesce into novel mitochondria-associated clusters during apoptosis. *J. Cell Biol.* **153**, 1265–1276 (2001). doi: [10.1083/jcb.153.6.1265](https://doi.org/10.1083/jcb.153.6.1265); pmid: [11402069](https://pubmed.ncbi.nlm.nih.gov/11402069/)
57. S. S. Smali, Y. T. Hsu, K. M. Sanders, J. T. Russell, R. J. Youle, Bax translocation to mitochondria subsequent to a rapid loss of mitochondrial membrane potential. *Cell Death Differ.* **8**, 909–920 (2001). doi: [10.1038/sj.cdd.4400889](https://doi.org/10.1038/sj.cdd.4400889); pmid: [11526446](https://pubmed.ncbi.nlm.nih.gov/11526446/)
58. G. Dewson, R. M. Kluck, Mechanisms by which Bak and Bax permeabilise mitochondria during apoptosis. *J. Cell Sci.* **122**, 2801–2808 (2009). doi: [10.1242/jcs.038166](https://doi.org/10.1242/jcs.038166); pmid: [19795525](https://pubmed.ncbi.nlm.nih.gov/19795525/)
59. S. W. G. Tait, D. R. Green, Mitochondria and cell death: Outer membrane permeabilization and beyond. *Nat. Rev. Mol. Cell Biol.* **11**, 621–632 (2010). doi: [10.15252/embj.201592789](https://doi.org/10.15252/embj.201592789); pmid: [26783364](https://pubmed.ncbi.nlm.nih.gov/26783364/)
60. L. Große *et al.*, Bax assembles into large ring-like structures remodeling the mitochondrial outer membrane in apoptosis. *EMBO J.* **35**, 402–413 (2016). doi: [10.15252/embj.201592789](https://doi.org/10.15252/embj.201592789); pmid: [26783364](https://pubmed.ncbi.nlm.nih.gov/26783364/)
61. R. Salvador-Gallego *et al.*, Bax assembly into rings and arcs in apoptotic mitochondria is linked to membrane pores. *EMBO J.* **35**, 389–401 (2016). doi: [10.15252/embj.201593384](https://doi.org/10.15252/embj.201593384); pmid: [26783362](https://pubmed.ncbi.nlm.nih.gov/26783362/)
62. H. Dussmann *et al.*, Single-cell quantification of Bax activation and mathematical modelling suggest pore formation on minimal mitochondrial Bax accumulation. *Cell Death Differ.* **17**, 278–290 (2010). doi: [10.1038/cdd.2009.123](https://doi.org/10.1038/cdd.2009.123); pmid: [19745831](https://pubmed.ncbi.nlm.nih.gov/19745831/)
63. D. A. Stroud *et al.*, Accessory subunits are integral for assembly and function of human mitochondrial complex I. *Nature* **538**, 123–126 (2016). doi: [10.1038/nature19754](https://doi.org/10.1038/nature19754); pmid: [27626371](https://pubmed.ncbi.nlm.nih.gov/27626371/)
64. L. Andreeva *et al.*, cGAS senses long and HMGB/TFAM-bound U-turn DNA by forming protein-DNA ladders. *Nature* **549**, 394–398 (2017). doi: [10.1038/nature23890](https://doi.org/10.1038/nature23890); pmid: [28902841](https://pubmed.ncbi.nlm.nih.gov/28902841/)
65. R. J. Youle, M. Karbowski, Mitochondrial fission in apoptosis. *Nat. Rev. Mol. Cell Biol.* **6**, 657–663 (2005). doi: [10.1038/nrm1697](https://doi.org/10.1038/nrm1697); pmid: [16025099](https://pubmed.ncbi.nlm.nih.gov/16025099/)
66. P. A. Parone *et al.*, Inhibiting the mitochondrial fission machinery does not prevent Bax/Bak-dependent apoptosis. *Mol. Cell Biol.* **26**, 7397–7408 (2006). doi: [10.1128/MCB.02282-05](https://doi.org/10.1128/MCB.02282-05); pmid: [17015472](https://pubmed.ncbi.nlm.nih.gov/17015472/)
67. J. R. Friedman *et al.*, ER tubules mark sites of mitochondrial division. *Science* **334**, 358–362 (2011). doi: [10.1126/science.1207385](https://doi.org/10.1126/science.1207385); pmid: [21885730](https://pubmed.ncbi.nlm.nih.gov/21885730/)
68. S. C. Lewis, L. F. Uchiyama, J. Nunnari, ER-mitochondria contacts couple mtDNA synthesis with mitochondrial division in human cells. *Science* **353**, aaf5549 (2016). doi: [10.1126/science.aaf5549](https://doi.org/10.1126/science.aaf5549); pmid: [27418514](https://pubmed.ncbi.nlm.nih.gov/27418514/)
69. R. K. Boyapati, A. Tamborska, D. A. Dorward, G.-T. Ho, Advances in the understanding of mitochondrial DNA as a pathogenic factor in inflammatory diseases. *Fluorescence* **6**, 169 (2017). doi: [10.12688/flourescence.10397.1](https://doi.org/10.12688/flourescence.10397.1); pmid: [28299196](https://pubmed.ncbi.nlm.nih.gov/28299196/)
70. S. Aguirre *et al.*, Dengue virus NS2B protein targets cGAS for degradation and prevents mitochondrial DNA sensing during infection. *Nat. Microbiol.* **2**, 17037 (2017). doi: [10.1038/nmicrobiol.2017.37](https://doi.org/10.1038/nmicrobiol.2017.37); pmid: [28346446](https://pubmed.ncbi.nlm.nih.gov/28346446/)
71. A. Sugiura, G.-L. McLelland, E. A. Fon, H. M. McBride, A new pathway for mitochondrial quality control: Mitochondrial-derived vesicles. *EMBO J.* **33**, 2142–2156 (2014). doi: [10.15252/embj.201488104](https://doi.org/10.15252/embj.201488104); pmid: [25107473](https://pubmed.ncbi.nlm.nih.gov/25107473/)
72. F. A. Ran *et al.*, Genome engineering using the CRISPR-Cas9 system. *Nat. Protoc.* **8**, 2281–2308 (2013). doi: [10.1038/nprot.2013.143](https://doi.org/10.1038/nprot.2013.143); pmid: [24157548](https://pubmed.ncbi.nlm.nih.gov/24157548/)
73. M. Raab *et al.*, ESCRT III repairs nuclear envelope ruptures during cell migration to limit DNA damage and cell death. *Science* **352**, 359–362 (2016). doi: [10.1126/science.1247611](https://doi.org/10.1126/science.1247611); pmid: [27013426](https://pubmed.ncbi.nlm.nih.gov/27013426/)
74. A. J. Lam *et al.*, Improving FRET dynamic range with bright green and red fluorescent proteins. *Nat. Methods* **9**, 1005–1012 (2012). doi: [10.1038/nmeth.2171](https://doi.org/10.1038/nmeth.2171); pmid: [22961245](https://pubmed.ncbi.nlm.nih.gov/22961245/)
75. D. S. Bindels *et al.*, mScarlet: A bright monomeric red fluorescent protein for cellular imaging. *Nat. Methods* **14**, 53–56 (2017). doi: [10.1038/nmeth.4074](https://doi.org/10.1038/nmeth.4074); pmid: [27869816](https://pubmed.ncbi.nlm.nih.gov/27869816/)
76. R. Fiolka, L. Shao, E. H. Rego, M. W. Davidson, M. G. L. Gustafsson, Time-lapse two-color 3D imaging of live cells with doubled resolution using structured illumination. *Proc. Natl. Acad. Sci. U.S.A.* **109**, 5311–5315 (2012). doi: [10.1073/pnas.1119262109](https://doi.org/10.1073/pnas.1119262109); pmid: [22431626](https://pubmed.ncbi.nlm.nih.gov/22431626/)
77. G. Ball *et al.*, SIMcheck: A toolbox for successful super-resolution structured illumination microscopy. *Sci. Rep.* **5**, 15915 (2015). doi: [10.1038/srep15915](https://doi.org/10.1038/srep15915); pmid: [26525406](https://pubmed.ncbi.nlm.nih.gov/26525406/)
78. J. W. Slot, H. J. Geuze, Cryosectioning and immunolabeling. *Nat. Protoc.* **2**, 2480–2491 (2007). doi: [10.1038/nprot.2007.365](https://doi.org/10.1038/nprot.2007.365); pmid: [17947990](https://pubmed.ncbi.nlm.nih.gov/17947990/)
79. B. S. Padman, M. Bach, G. Ramm, An improved procedure for subcellular spatial alignment during live-cell CLEM. *PLOS ONE* **9**, e95967 (2014). doi: [10.1371/journal.pone.0095967](https://doi.org/10.1371/journal.pone.0095967); pmid: [24755651](https://pubmed.ncbi.nlm.nih.gov/24755651/)
80. S. Preibisch, S. Saalfeld, P. Tomancak, Globally optimal stitching of tiled 3D microscopic image acquisitions. *Bioinformatics* **25**, 1463–1465 (2009). doi: [10.1093/bioinformatics/btp184](https://doi.org/10.1093/bioinformatics/btp184); pmid: [19346324](https://pubmed.ncbi.nlm.nih.gov/19346324/)
81. V. Kaynig, B. Fischer, E. Müller, J. M. Buhmann, Fully automatic stitching and distortion correction of transmission electron microscope images. *J. Struct. Biol.* **171**, 163–173 (2010). doi: [10.1016/j.jsb.2010.04.012](https://doi.org/10.1016/j.jsb.2010.04.012); pmid: [20450977](https://pubmed.ncbi.nlm.nih.gov/20450977/)

ACKNOWLEDGMENTS

We thank A. Taylor, L. Shao, F. Babayekhorasani, and S. Khuon for microscopy assistance; B. Howden for personnel support; C. De Nardo for administrative support; and D. C. S. Huang and F. Kraus for providing constructs and cell lines. **Funding:** Supported by an Australian Federal Government Postgraduate Award (K.M.); Project Grants (1077750, 1106471, 1078924, 1083077), Program Grants (1016647, 1113577, 1113133), Fellowships (1063008, B.T.K.; 1117089, G.L.), an ARC Future Fellowship (160100063, M.L.), an ARC Discovery Grant (DP16012176, M.T.R.), and an Independent Research Institutes Infrastructure Support Scheme Grant (361646) from the Australian National Health and Medical Research Council (NHMRC); the Australian Cancer Research Fund; and a Victorian State Government Operational Infrastructure Support Grant. The Advanced Imaging Center at Janelia Research Campus is jointly supported by the Howard Hughes Medical Institute and the Gordon and Betty Moore Foundation. The Monash Ramaciotti Centre for Cryo-Electron Microscopy is supported by the Ramaciotti Foundation (CD11/1958) and the Australian Research Council (LE120100090 and LE100100165). **Author contributions:** K.M., J.M.H., N.D.G., L.L., and K.L.R. performed LLSM and 3D-SIM microscopy experiments. K.M. and S.D. performed confocal microscopy experiments. V.O. and G.R. performed EM experiments; B.S.P. performed CLEM experiment. L.W., K.M., B.T.K., M.L., N.D.G., S.C., and M.D. analyzed data. K.M., T.L.S., C.S., L.L., G.D., and R.M.L. performed cell culture and related experiments. L.D.O., R.L., M.T.R., and H.S.C. provided reagents. B.T.K., K.M., and M.F.v.D. conceived the project and planned experiments. M.F.v.D., M.T.R., G.D., K.L.R., G.L., T.L.C., J.M.H., S.C., G.R., and M.L. contributed insightful discussions. K.M. and B.T.K. wrote the manuscript, and all authors contributed to its revision. **Competing interests:** All authors declare no competing interests. **Data and materials availability:** All data and custom analysis scripts are available in the manuscript or the supplementary materials.

SUPPLEMENTARY MATERIALS

www.sciencemag.org/content/359/6378/eaao6047/suppl/DC1
Figs. S1 to S6
Code Files S1 and S2

8 August 2017; accepted 24 January 2018
10.1126/science.aao6047

BAK/BAX macropores facilitate mitochondrial herniation and mtDNA efflux during apoptosis

Kate McArthur, Lachlan W. Whitehead, John M. Heddlestone, Lucy Li, Benjamin S. Padman, Viola Oorschot, Niall D. Geoghegan, Stephane Chappaz, Sophia Davidson, Hui San Chin, Rachael M. Lane, Marija Dramicanin, Tahnee L. Saunders, Canny Sugiana, Romina Lessene, Laura D. Osellame, Teng-Leong Chew, Grant Dewson, Michael Lazarou, Georg Ramm, Guillaume Lessene, Michael T. Ryan, Kelly L. Rogers, Mark F. van Delft and Benjamin T. Kile

Science **359** (6378), eaao6047.
DOI: 10.1126/science.aao6047

The great escape

Mitochondrial DNA (mtDNA) is a potent damage-associated molecular pattern that, if it reaches the cytoplasm or extracellular milieu, triggers innate immune pathways. mtDNA signaling has been implicated in a wide range of diseases; however, the mechanisms of mtDNA release are unclear, and the process has not been observed in real time thus far. McArthur *et al.* used live-cell lattice light-sheet microscopy to look at mtDNA release during intrinsic apoptosis. Activation of the pro-death proteins BAK and BAX resulted in the formation of large macro-pores in the mitochondrial outer membrane. These massive holes caused the inner mitochondrial membrane to balloon out into the cytoplasm, resulting in mitochondrial herniation. This process allowed the contents of the mitochondrial matrix, including mtDNA, to escape into the cytoplasm.

Science, this issue p. eaao6047

ARTICLE TOOLS

<http://science.sciencemag.org/content/359/6378/eaao6047>

SUPPLEMENTARY MATERIALS

<http://science.sciencemag.org/content/suppl/2018/02/21/359.6378.eaao6047.DC1>

REFERENCES

This article cites 81 articles, 27 of which you can access for free
<http://science.sciencemag.org/content/359/6378/eaao6047#BIBL>

PERMISSIONS

<http://www.sciencemag.org/help/reprints-and-permissions>

Use of this article is subject to the [Terms of Service](#)